

# Mitotic waves in frog egg extracts: Transition from phase waves to trigger waves

Owen Puls<sup>1,2,\*</sup>, Daniel Ruiz-Reynés<sup>3,4,\*</sup>, Franco Tavella<sup>2,5</sup>, Minjun Jin<sup>2,5</sup>, Yeonghoon Kim<sup>2</sup>, Lendert Gelens<sup>3,†,‡</sup>, and Qiong Yang<sup>1,2,5,†,§</sup>

<sup>1</sup>Department of Physics, University of Michigan, Ann Arbor, MI 48109, USA.

<sup>2</sup>Department of Biophysics, University of Michigan, Ann Arbor, MI 48109, USA.

<sup>3</sup>Laboratory of Dynamics in Biological Systems, KU Leuven, Department of Cellular and Molecular Medicine, University of Leuven, B-3000 Leuven, Belgium.

<sup>4</sup>IFISC (CSIC-UIB). Instituto de Física Interdisciplinar y Sistemas Complejos, E-07122 Palma de Mallorca, Spain.

<sup>5</sup>Department of Computational Medicine and Bioinformatics, University of Michigan, Ann Arbor, MI 48109, USA.

\*contributed equally

†contributed equally

‡lendert.gelens@kuleuven.be

§qiongy@umich.edu

## ABSTRACT

1 Cyclin-dependent kinase 1 (Cdk1) activity rises and falls throughout the cell cycle, a cell-autonomous  
2 process known as mitotic oscillations. These oscillators can synchronize when spatially coupled, providing a  
3 crucial foundation for rapid synchronous divisions in large early embryos like *Drosophila* (~ 0.5 mm) and  
4 *Xenopus* (~ 1.2 mm). While diffusion alone cannot achieve such long-range coordination, recent studies  
5 have proposed two types of mitotic waves, phase and trigger waves, to explain the phenomena. How the  
6 waves establish over time for efficient spatial coordination remains unclear. Using *Xenopus laevis* egg  
7 extracts and a Cdk1 FRET sensor, we observe a transition from phase waves to a trigger wave regime in an  
8 initially homogeneous cytosol. Adding nuclei accelerates such transition. Moreover, the system transitions  
9 almost immediately to this regime when externally driven by metaphase-arrested extracts from the boundary.  
10 Employing computational modeling, we pinpoint how wave nature, including speed-period relation, depends  
11 on transient dynamics and oscillator properties, suggesting that phase waves appear transiently due to the  
12 time required for trigger waves to entrain the system and that spatial heterogeneity promotes entrainment.  
13 Therefore, we show that both waves belong to a single biological process capable of coordinating the cell  
14 cycle over long distances.

## INTRODUCTION

15 Cell division, one of the most important processes in biology, is regulated by a well-studied pacemaker  
16 oscillator centered on the cyclin B-Cdk1 complex, known as the mitotic clock<sup>1,2</sup> (Fig. 1a). The mitotic cell  
17 cycle, specifically the DNA-replication-and-division cycle, undergoes a sequence of events in which cells  
18 replicate DNA and partition the copies into daughter cells such that each daughter receives precisely one  
19 copy of the genome<sup>3</sup>.

20 In the early embryogenesis of organisms such as *Xenopus* or *Drosophila*, cells initially proceed through a  
21 series of fast divisions<sup>4,5</sup>. These mitotic cycles lack many features of mature cells—e.g., gap phases, cell  
22 cycle checkpoints, and zygotic gene transcription—which only arise after the mid-blastula transition (MBT)<sup>6</sup>.  
23 For this reason, it is key for these cycles to remain roughly synchronized prior to MBT, even though some  
24 desynchronization is tolerated<sup>7</sup>. Throughout this process, mitotic events occur within minutes of each other.  
25 However, due to the large cell size in such embryos, diffusion alone remains far too slow to synchronize the  
26 system: such a process would take multiple hours, not minutes<sup>8–12</sup>.

27 Previous studies have identified waves of mitotic events, both *in vitro* and *in vivo*, which propagate  
28 at speeds sufficiently high to communicate across the lengths of the embryo<sup>8,9</sup>. Trigger waves ( $\sim 40$ -  
29  $60 \mu\text{m}/\text{min}$ ), resulting from the coupling of diffusion and local dynamics<sup>10,11</sup>, were first shown to coordinate  
30 mitosis in *Xenopus*, using nuclear envelope breakdown (NEB) to illustrate their propagation after a few early,  
31 largely synchronous cycles<sup>8</sup>. Subsequent work revealed that the nucleus itself serves as the pacemaker for  
32 these waves, locally accelerating oscillations possibly by aggregating cell cycle regulators and thus driving  
33 waves<sup>13,14</sup>. This aggregating mechanism was later confirmed in individual oscillating microemulsions<sup>15</sup>.  
34 However, the classical trigger wave mechanism may not be the sole contributor to the fast wave propagation  
35 observed in the early embryos.

36 Like *Xenopus* and other metazoans, the fruit fly embryo undergoes a series of rapid, roughly synchronous  
37 (and in this case, syncytial) divisions post-fertilization<sup>6</sup>. However, *Drosophila* embryos display waves of  
38 mitotic completion that traverse the entirety of the embryo (hundreds of microns) in mere minutes at early  
39 stages, with speeds much faster ( $\sim 100 \mu\text{m}/\text{min}$ ) than what could be achieved by traditional trigger wave  
40 models<sup>9</sup>. Moreover, embryos exhibit distinct spatial dynamics that forgo the classical picture of a stable  
41 regime invading into and promoting a metastable regime<sup>10,11</sup>. Instead, spatial gradients in Cdk1 activity are  
42 largely preserved, while the overall levels are swept upwards<sup>16</sup>.

43 Vergassola *et al.* propose that a distinct phenomenon termed “sweep” waves (or “phase” waves in

44 our terminology, as accepted in a subsequent review<sup>12</sup>) is responsible for the ultra-fast waves observed *in*  
45 *vivo*<sup>12,16</sup>. Phase waves appear to spread due to local phase gradients but are not actively spread by mutual  
46 interactions, in contrast with trigger waves, which do propagate through a coupling of diffusion and local  
47 reactions<sup>8-12</sup>. The authors suggest that a time-dependent sweeping-up of Cdk1 activity leads to wave-like  
48 behavior spreading at scales faster than trigger waves, consistent with phase waves. Interestingly, the authors  
49 observe that the period of the oscillator lengthens for late cycles (due to Chk1) and propose a potential link  
50 between phase and trigger waves through this mechanism<sup>16</sup>. More recently, the authors speculate that such a  
51 transition could also exist in *Xenopus* and called for direct measurements of Cdk1 activity to resolve this  
52 open question<sup>17</sup>.

53 In this work, we present direct evidence of mitotic waves in *Xenopus* using a FRET sensor that measures  
54 the ratio of activity between Cdk1 and its opposing phosphatase. We show that waves of Cdk1 activity  
55 can form spontaneously in the absence of nuclear pacemakers, sharing the fundamental nature of the  
56 classical chemical waves in a Belousov-Zhabotinsky (BZ) reaction-diffusion system. We investigate the  
57 time-dependent behavior of mitotic waves in *Xenopus* extracts, revealing a transition from phase-wave-like  
58 to trigger-wave-like patterns over time, and as a result, offer the connecting thread between these phenomena.  
59 We also probe the role of nuclei in wave propagation, showing that in addition to acting as pacemakers,  
60 nuclei accelerate the entrainment of the system to the trigger wave regime. Building on the findings in these  
61 experiments, we then propose a novel method for generating directed waves *in vitro*, which reinforces the  
62 notion of entrainment explicitly. In short, we use a reservoir of active Cdk1 to drive waves through the  
63 oscillating medium. Taken together, we offer a generalized picture of the interplay between phase and trigger  
64 waves and the role of heterogeneities in the spatial coordination of *Xenopus laevis*' early embryogenesis.

## RESULTS

### Mitotic waves transition from fast phase waves to slower trigger waves

65 We leverage *in vitro* cell-free extracts to characterize mitotic waves in *Xenopus*. A schematic view of the  
66 experimental setup is presented in Fig. 1a. Cycling extracts are prepared following the protocol described  
67 in previous studies<sup>18,19</sup>. Instead of relying on downstream events such as NEB, we employ a FRET  
68 sensor to report the Cdk1 kinase activity, which allows us to directly visualize mitotic waves over time in  
69 *Xenopus*<sup>15</sup>. Cycling extracts supplemented with the Cdk1 FRET sensor are then loaded into ~ 5-10 mm long  
70 Teflon-coated tubes, submerged under mineral oil, and imaged using time-lapse epifluorescent microscopy.

71 In a representative experiment (Fig. 1b; Mov. 1), the FRET signal is represented by a heatmap with cool  
72 colors corresponding to low Cdk1 activity, and warm colors to high activity. High activity regions can be  
73 clustered together via peak detection, allowing us to individualize wavefronts. Two wavefronts at different  
74 time regions are highlighted for comparison (Fig. 1b, top, white lines). Qualitatively, one can observe a  
75 difference between early time patterns that are largely synchronous and fast moving (Fig. 1b, top, dashed  
76 white line), and later time patterns which form linear fronts (Fig. 1b, top, solid white line). The explicit time  
77 evolution of the FRET signal is also depicted for a small slice (at position  $x = 10$  mm; Fig. 1b, bottom).  
78 When plotting the FRET ratio spatial profile over consecutive frames for early and late cycles (Fig. 1c), we  
79 observe clear changes in spatial profiles over time. Early patterns ( $T_1$ : 0-60 min) resemble phase waves: a  
80 roughly uniform upswing in activity, and preservation of local peaks and spatial gradients (Fig. 1c, top),  
81 sharing similar features as those reported in Hayden *et al.*<sup>17</sup>. Conversely, at late times ( $T_2$ : 1000-1200 min),  
82 the system exhibits clearly linear, trigger-wave-like fronts, characterized by traveling pulses (Fig. 1c, bottom).  
83 This implies a transition from phase waves at early, fast cycles, to trigger waves at late, slower cycles.

84 To quantify this transition, we choose to measure the period and wave speed. The period is calculated  
85 as the peak-to-peak time between wavefronts (Fig. 1b, bottom; Fig. 1d, top). Since the speed of early time  
86 patterns is often infinite at this resolution, we calculate the instantaneous derivative (slope,  $dt/dx$ ) of the  
87 interpolated kymograph, using its reciprocal as an indicator of wave speed. In both cases, we estimate the  
88 kernel density (KDE) of the data over time. We observe that the LOWESS estimate for the period closely  
89 follows the peaks in density (Fig. 1d, top). However, this is not the case for the slope. The slope density  
90 shows low values at early times, high values at later times, and a mixture in between, suggesting a transition  
91 between different types of waves (Fig. 1d, middle). Wave speeds are obtained by inverting the LOWESS  
92 slope estimate, showing a monotonic decrease over time (Fig. 1d, bottom). The decrease in wave speed  
93 seems to follow a two-step process with an initial fast decay and a slower transition to a terminal speed ( $v_t$ ).  
94 We quantify this transition following a moving horizon fitting algorithm (see Methods). Briefly, we find the  
95 potential transition starting time point ( $\tau_0$ ) that gives the best fit for exponential decay of the signal at late  
96 times (Fig. S1). This time point tells us when waves start to relax exponentially towards the trigger wave  
97 state of later times. From the fitted exponential function, we extract a relaxation time scale ( $\Delta\tau$ ) and thus  
98 fully quantify how long the system takes to transition between each state. For this data, wave speeds start to  
99 decay exponentially after  $\tau_0 = 462$  min (Fig. 1d, bottom, dashed blue line) with a relaxation time scale of  
100  $\Delta\tau = 528$  min (Fig. 1d, bottom, red arrow). Interestingly, despite changes in period and wave speed, the

101 FRET ratio maximum activation rate ( $dA/dt$ ), calculated as the largest time derivative of the FRET ratio per  
102 cycle, remains relatively constant for the duration of the experiment (Fig. S2).

103 When combined, our measurements reveal that the wave speed monotonically decreases as the cell cycle  
104 period lengthens (Fig. 1e). At early times (before  $\tau_0$ ), the period is short, and the system exhibits phase waves  
105 at diversified speeds of 400-100  $\mu\text{m}/\text{min}$ , which are much faster than trigger waves. However, these transients  
106 eventually die off as the system transitions to a regime quasi-dominated by trigger waves (100-50  $\mu\text{m}/\text{min}$ ).  
107 This speed-period relation also appears to confirm a sweep-to-trigger transition, reported in fly embryos  
108 upon genetic perturbations<sup>17</sup>, though in this case, we directly observed the transition as an inherent temporal  
109 evolution of the system, independent of external induction, thus bridging our understanding of mitotic waves  
110 between different model systems.

### **A generic cell cycle model shows that transient dynamics explains the observed phase to trigger wave transition**

111 The observed transition from fast phase waves to slow trigger waves could be a result of two time-dependent  
112 factors. On the one hand, we observed period lengthening, which suggests a potential time dependence in  
113 the intrinsic biochemical properties of the oscillator. On the other hand, if we consider trigger waves as the  
114 attractor state of a dynamical system, the transition may imply a relaxation towards this state, a time-evolving  
115 process that necessitates a finite amount of time for a transient state (from a wide variety of initial conditions)  
116 to establish into a stable solution (attractor).

117 We turn to mathematical modeling to quantify the effect of these two hypothetical contributions to the  
118 wave dynamics we observed. We use a cell-cycle model introduced by Yang and Ferrell<sup>20</sup> and then later  
119 extended by Chang and Ferrell<sup>8</sup> to describe mitotic waves. The model describes the time evolution of  
120 active (denoted as  $a$ ) and total cyclin B-Cdk1 (denoted as  $c$ ) concentration (Eqs. (1) and (2)). Cyclin B  
121 is synthesized at a rate  $k_s$  and then rapidly binds to Cdk1. The activity of the cyclin B-Cdk1 complex is  
122 regulated by phosphatase Cdc25, which activates the complex by dephosphorylation, and kinases Wee1 and  
123 Myt1, which deactivate the complex by phosphorylation. Finally, high Cdk1 activity leads to the activation  
124 of anaphase-promoting complex/cyclosome (APC/C), which targets cyclin B for degradation (Fig. 1a).  
125 The reaction rates are described by ultrasensitive response curves dependent on the cyclin B-Cdk1 activity  
126 and parameterized based on experiments<sup>20</sup>. Diffusion is incorporated into the model to simulate spatially  
127 extended dynamics.

128 To replicate the observed period lengthening, we introduce an explicit time dependence to the mitotic

129 regulatory network. Adopting a methodology similar to Rombouts and Gelens<sup>21,22</sup>, we explore how the  
130 model parameters influence the period and activation rate ( $da/dt$ ), which we use to compare to their  
131 experimentally observable counterparts (period and maximum activation rate  $dA/dt$ , extracted from the  
132 FRET signal time traces, respectively). We further modify the model equations with dimensionless factors  $\alpha$ ,  
133  $\beta$ ,  $\eta$  to examine the significance of the key network components (Fig. 2a). Factor  $\alpha$  scales the activation  
134 and inactivation rates of Cdk1, which constitute the bistable switch at the mitotic network core. Numerical  
135 simulation shows that the period remains almost unaffected by  $\alpha$  (Figs. 2a and S3, left). Factor  $\beta$  controls  
136 how fast cyclin B is synthesized and degraded, thus being fundamental for driving oscillations through the  
137 bistable trigger and negative feedback. Scaling  $\beta$  leads to a modulation of the period (interphase lengthening)  
138 and mostly unchanged activation rate (Figs. 2a and S3, middle). Finally, factor  $\eta$  corresponds to a global time  
139 scaling, thus affecting every observable (Figs. 2a and S3, right). Out of the three modifications, changing  
140  $\beta$  produces the most similar behavior to our experimental observations: the period lengthens without a  
141 significant change in activation rate. Therefore, by dialing the bistable trigger over time (decreasing  $\beta$ ), we  
142 obtain a phenomenological model that reproduces the observed cell cycle behaviors.

143 To model relaxation dynamics, we incorporate a heterogeneous spatial profile of the cyclin synthesis rate  
144  $k_s(x)$ . The loci with smaller periods in this profile (corresponding to larger values of  $k_s(x)$ ) can act as trigger  
145 wave sources, as explored in previous works for pointlike sources<sup>21,22</sup>.

146 Thus, we perform numerical simulations incorporating these two contributions: a time-dependent  $\beta(t)$   
147 (Fig. 2b, top) and a noisy  $k_s(x)$  distributed across space (Fig. 2b, left). The diffusion rate is set to be  
148  $240 \mu\text{m}^2/\text{min}$ , compatible with a rate reported in the fly embryo<sup>9</sup>, to reproduce the wave speed at the end of  
149 the extract lifetime ( $\gtrsim 1,000$  min). The simulated kymograph in Fig. 2b captures both the period lengthening  
150 of waves and the gradual formation of slow linear fronts that resemble the qualitative observations from  
151 experiments. The formation of linear fronts is influenced by the noise level, denoted by  $A_k$  (see Methods  
152 for the definition); comparing two simulations with different levels of spatial noise, we find that large  
153 heterogeneity ( $A_k = 0.05$ ) entrains the system more rapidly than small heterogeneity (0.025), leading to a  
154 faster reduction to a wave speed that is characteristic of a trigger wave (Fig. 2c).

155 Applying the same analysis used for experimental data allows us to plot the speed-period relation for  
156 various heterogeneity levels (Fig. 2d). Keeping in mind that the period is a monotonically increasing function  
157 of time, we observe that the transition from phase waves to trigger waves happens both earlier ( $\tau_0$ , blue  
158 dots) and faster ( $\Delta\tau$ , red regions, end with black dots) as the heterogeneity rises.  $A_k = 0.03$  gives a result

159 that quantitatively agrees with experiments, characterized by a two-step decay with  $\tau_0 = 579$  min and  
160  $\Delta\tau = 482$  min.

161 Finally, we analyze the dependence of the transition time scales on the level of heterogeneity  $A_k$  (Fig. 2e).  
162 Increasing spatial heterogeneity significantly speeds up the transition to trigger waves, occurring both earlier  
163 (Fig. 2e, blue) and faster (Fig. 2e, red). Additionally, we find that suppressing the period elongation does  
164 not affect the speedup resulting from increased spatial heterogeneity (Fig. S4). Therefore, the dominant  
165 effect in the transition from fast phase waves to slow trigger waves is the finite relaxation time required by  
166 traveling waves to establish themselves. All in all, our modeling suggests that this transition can be sped up  
167 by introducing spatial heterogeneity into our system.

### **Nuclei speed up the transition from phase waves to trigger waves**

168 The question then arises: how can we incorporate spatial heterogeneity in our experimental system? One  
169 possible approach is to introduce nuclei into the system. Nuclei can drive wave formation by acting as  
170 pacemakers<sup>13,14</sup>. Modeling work demonstrates that the inclusion of pacemakers, whether explicitly or  
171 implicitly, drives waves at a frequency that correlates with pacemaker activity, with wave speed being  
172 dependent on this driving frequency<sup>8,13,21–23</sup>. Therefore, compartmentalizing the cytosol by introducing  
173 nuclei might affect how fast the system transitions from phase to trigger waves.

174 We supplement extracts with demembrated *Xenopus* sperm DNA (+XS), a method commonly used in  
175 the field to reconstitute nuclei<sup>8,13–15</sup>. A representative kymograph of this experiment shows clear wavefronts  
176 spanning the whole length of the tube (Fig. 3a, top). The zoomed-in region shows individual nuclei forming  
177 during interphase, importing active Cdk1 prior to NEB, and disappearing upon NEB (Fig. 3a, bottom). Even  
178 at this relatively coarse timescale (at 5-min time intervals), we observe the pacemaker nucleus accumulating  
179 more active Cdk1 than its neighbors and thereby undergoing NEB earlier (Fig. 3a, bottom, red arrows).  
180 After NEB, active Cdk1 fills the local region, and pulse-like waves propagate in both directions (Fig. 3a,  
181 bottom). Similar to the case without nuclei, the spatial profiles clearly indicate that at early times, the patterns  
182 resemble phase waves and at later times, trigger waves (Fig. 3b; Mov. 2). In other words, despite nuclei  
183 visibly forming at early times, we observe a comparable sweeping up of activity, though the effect is much  
184 noisier and punctuated by peaks associated with the nuclei themselves throughout the tube (Fig. 3b, top). As  
185 time progresses, trigger waves become dominant, and the system exhibits clear traveling pulses from the  
186 dominating pacemaker nucleus (Fig. 3b, bottom).

187 Repeating the same workflow described previously for this compartmentalized system, we find qual-

188 itatively similar behavior for each of the relevant quantities: the slope (Fig. 3c) and period (Fig. 3d, top)  
189 both increase over time, while the maximum activation rate remains constant (Fig. S2c). Despite the time  
190 evolution of the period being similar between the two conditions ( $\pm$ XS), the slope for waves with nuclei  
191 consistently exceeds that of waves without nuclei within the 1200-minute observation window (Fig. 3c),  
192 indicating a potential impact of nuclei on the wave propagation dynamics. To quantify this, we again measure  
193 the entrainment time from the exponential fitting (Fig. 3d, bottom). We obtain an entrainment time of  
194  $\tau_0 = 115$  min and  $\Delta\tau = 157$  min, which is faster than that of the non-nuclei system, indicating a speedup  
195 in the transition to trigger waves caused by the presence of nuclei. Interestingly, the fit for both conditions  
196 produces a terminal speed close to  $40 \mu\text{m}/\text{min}$ , suggesting a common long-term behavior that agrees with  
197 speeds previously reported<sup>8,13</sup>. The difference in the entrainment time between the two systems is made  
198 clearer when considering the speed-period relation (Fig. 3e). As shown, the transient phase waves give way  
199 to trigger waves much more rapidly than in the systems without nuclei, as indicated by a decay in speed  
200 that begins earlier. The slight increase in speed at late times in the nuclei case is likely due to extract death.  
201 Despite this, it is clear that the addition of sperm DNA (nuclei) causes the system to admit trigger waves  
202 earlier in time, but also “earlier” in terms of period. This reinforces the idea that wave speed changes due to  
203 transient effects, rather than being driven by changes in period.

204 Our results show that nuclei speed up the entrainment of the system to the trigger wave regime. Nuclei  
205 act as pacemakers<sup>13,14</sup>, providing nucleation points for singular wavefronts. Supported by our computational  
206 analysis, we extend this notion to argue that the nuclei play a broader role in bringing the system out of  
207 the transitory, less-specified phase wave regime and into the well-defined, classical trigger wave regime.  
208 In systems without nuclei, patterns remain diffusive and exhibit fast speeds. Over time, trigger waves do  
209 develop, albeit slowly. Conversely, systems with nuclei develop trigger waves earlier and more frequently.  
210 Consequently, the former displays fast speeds that slowly decrease, while the latter displays speeds that  
211 quickly decay and follow a trigger wave speed-period relation.

### **Driving waves with metaphase-arrested extract speeds up the transition to trigger waves with and without nuclei**

212 To further understand the entrainment of mitotic waves, we set out to drive waves explicitly by a cytostatic-  
213 factor (CSF) extract, similar to a previous study that drove an apoptotic signal through a tube of interphase  
214 extract using a reservoir of apoptotic-arrested extract<sup>24</sup>.

215 CSF extract, a metaphase-arrested extract, is derived from inactivated eggs arrested at meiosis-II<sup>25,26</sup>.

216 While the biological details of CSF arrest remain to be elucidated, the field largely agrees that the Emi family  
217 of proteins plays a major role by inhibiting APC/C, with other studies also highlighting the involvement of  
218 the Mos-MAPK pathway in CSF arrest<sup>27,28</sup>. Despite these uncertainties, CSF extracts consistently exhibit  
219 and maintain high Cdk1 activity unless released from arrest<sup>29</sup>. Moreover, these extracts can be frozen and  
220 stored for many months, providing a reliable source of stable high-Cdk1-activity extract<sup>30</sup>. Due to the  
221 self-promoting activity of Cdk1 in the mitotic circuit, supplementing oscillating extract with CSF is expected  
222 to result in forced activation and consequent propagation of traveling mitotic waves (Fig. 4a).

223 To validate this setup, we create a bistable traveling wave using CSF extracts and interphase extracts.  
224 Both extracts are prepared following standard protocols in the field<sup>29-31</sup>. We observe that briefly dipping an  
225 interphase-extract-filled tube into a CSF reservoir allows the high Cdk1 activity in CSF extracts to excite  
226 a traveling pulse of Cdk1 activity in the tube (Fig. 4b; Mov. 3). Waves propagate at a consistent speed  
227 of  $40 \pm 2$   $\mu\text{m}/\text{min}$ , in agreement to previously measured mitotic trigger waves in cycling extracts<sup>8,13,14</sup>.  
228 Visualizing the spatial profiles by shifting the FRET ratio reveals a clear traveling peak of activity, confirming  
229 the presence of trigger waves (Fig. 4c). This experiment demonstrates the efficacy of using CSF extracts as  
230 an explicit source to drive waves.

231 We thus applied the CSF extracts to drive tubes filled with cycling extract with or without sperm DNA  
232 added; in both cases, we observed the mitotic arrested region persistently drives multiple cycles of Cdk1  
233 activity waves throughout the tube (Fig. 4d; Mov. 4 and Mov. 5). Similar to the non-driven experiments,  
234 wavefronts appear as pulses of high Cdk1 activity, regardless of the presence of nuclei, validating the  
235 emergence of trigger waves (Fig. 4e).

236 Applying the same analysis pipeline as before, we study how period and wave speed change over time.  
237 Initially, both conditions show a slight decrease in the oscillation period, likely due to the diffusing influence  
238 of CSF, followed by a “typical” period elongation (Fig. S5a). While the observed behavior is qualitatively  
239 similar, the two conditions show a difference in the magnitude of the change in period despite experiencing  
240 the same driving force (Fig. S5b). When measuring the wave speed in terms of slopes, we find that the  
241 system with nuclei has higher values than their non-nuclei counterparts (Fig. S5c), matching what we observe  
242 in the non-driven system (Fig. 3c). This is likely due to the longer periods in the system with nuclei, but also  
243 suggests a possible difference at the level of wave propagation.

244 Our time scale analysis of wave speed reveals that the entrainment time for the condition with nuclei  
245 (+XS,  $\tau_0 = 45$  min,  $\Delta\tau = 83$  min) is shorter than without (-XS,  $\tau_0 = 146$  min,  $\Delta\tau = 411$  min) (Fig. 4f).

246 The fact that entrainment times for driven waves are significantly shorter than their non-driven counterparts  
247 (Fig. 4f,  $\pm XS$ , as compared to Fig. 3d,  $\pm XS$ ) seems to point to a cumulative effect from multiple pacemakers:  
248 both the CSF and nuclei contribute to entrainment. Interestingly, the entrainment time for the CSF-driven  
249 case without nuclei ( $-XS/+CSF$ ,  $\tau_0 = 146$  min,  $\Delta\tau = 411$  min) is still longer than the undriven case with  
250 nuclei ( $+XS/-CSF$ ,  $\tau_0 = 115$  min,  $\Delta\tau = 157$  min). It is plausible a set of multiple, but theoretically weaker,  
251 pacemakers could entrain the system faster given a distributed effect throughout space. In addition, the  
252 relaxation time scale for the CSF-driven case without nuclei ( $\Delta\tau = 411$  min) is not shortened significantly  
253 compared to the non-driven experiment ( $\Delta\tau = 528$  min), although CSF driving brings systems to initiate the  
254 transition more quickly ( $\tau_0 = 146$  and  $462$  min, respectively). In contrast, the presence of nuclei shortens both  
255 the initiation time and the relaxation time. This discrepancy underscores a fundamental biological difference  
256 in how CSF and nuclei contribute to entrainment, which is worth further investigation. Additionally, the  
257 fitted terminal speed  $30 \mu\text{m}/\text{min}$  matches what we and others observed previously<sup>8,13,14</sup>.

258 Importantly, driving the system in this way explicitly entrains the system to the trigger wave regime,  
259 quickly and permanently. The phase waves of early times start to transition to trigger waves within two or  
260 three cycles and propagate across the entirety of the tube. These waves appear to follow a clear speed-period  
261 relation, distinct from the undriven case (Fig. 4g). In both cases, we see a fast decrease in speed with small  
262 changes in period that lead to a smooth approach to terminal speed (Fig. 4g). In this way, driving the system  
263 elucidates a clear difference between the transients—and possible phase waves—of early times and trigger  
264 waves, and reinforces the notion of entrainment explicitly.

### **The presence of phase waves and trigger waves depends on spatial heterogeneities in initial conditions and system parameters**

265 There is a key conceptual distinction between phase waves and trigger waves. While information transmission  
266 by phase waves is nearly absent and synchrony is only maintained when the initial phase difference is small,  
267 trigger waves transmit information over long distances. The mechanisms underlying the two kinds of waves  
268 are also different. Although both appear in oscillatory systems, trigger waves require timescale separation  
269 and spatial coupling commonly mediated by diffusion. Timescale separation in our experiments is naturally  
270 present due to the rapid activation of cyclin B-Cdk1 compared to cyclin buildup from synthesis. It is this rapid  
271 activation that excites neighboring regions through protein diffusion and triggers a sustained propagation  
272 of the wave. In contrast, phase waves appear as a result of a small delay in the activation time of adjacent  
273 positions, creating a structured phase difference that takes the appearance of a wave. Another important

274 difference is in the speed of the wave and its stability. The speed of a trigger wave is uniquely defined by the  
275 properties of the underlying oscillator and diffusion, and it is said to be stable because waves with different  
276 propagation speeds will converge to the stable one. Conversely, a phase wave is not stable, it can appear at  
277 any speed, and diffusion will attenuate phase differences with time until the system oscillates synchronously.

278 To demonstrate the difference, we use numerical simulations to initiate a trigger wave by introducing  
279 a period difference at the center of the spatial domain with spatially homogeneous levels of activity as the  
280 initial condition (Fig. 5a, (i)). In contrast, we initiate a phase wave by keeping the period fixed in space and  
281 asserting an initial condition where there is a linear difference in the phase of the oscillator that decreases  
282 as one moves far from the central position (Fig. 5a, (ii)). Then we explore the robustness of both systems  
283 by reducing the timescale separation of the oscillator (Fig. 5a, (iii, iv)), where the timescale separation is  
284 controlled by factor  $\alpha$  for relaxation-like ( $\alpha = 1$ , Fig. 2a, left, black lines) and sinusoidal ( $\alpha < 1$ , Fig. 2a,  
285 left, red lines) oscillations. Quantifying the shapes of wavefronts at late times with the fit  $x = d + vt^\gamma$ , we  
286 obtain the dependence of the trigger-wave-likeness on  $\alpha$ , summarized in Fig. 5b. We found that only when  
287 the oscillations are relaxation-like, indicated by larger values of  $\alpha$ , trigger waves establish in space in a  
288 stable manner, entraining the oscillatory background and displaying a linear front ( $\gamma = 1$ , Fig. 5a, (i)), while  
289 low values of  $\alpha$ , which correspond to sinusoidal oscillations, lead to a curved front ( $\gamma > 1$ , Fig. 5a, (iii)).  
290 Increasing timescale separation with  $\alpha$  also amplifies the penetration depth of the trigger wave into the  
291 medium<sup>21,22</sup>, as shown in the long-time behavior, comparing Fig. 5a, (i) and (iii). On the other hand, phase  
292 waves do not change with the timescale separation, comparing Fig. 5a, (ii) and (iv). The spatially averaged  
293 wave speed, measured at the wavefront segments in the kymograph (Fig. 5a, (i), red lines), converges to the  
294 stable value expected for trigger waves (Fig. 5c, (i)); in contrast, the speed for phase waves (Fig. 5a, (ii), red  
295 lines) increases with time as the oscillations synchronize (Fig. 5c, (ii)).

296 Together, our numerical simulations (Figs. 2 and 5) suggest a crucial role of spatial heterogeneity in  
297 the phase-to-trigger wave transition, confirmed by our experimental observations, which we recapitulate in  
298 Fig. 6. First, disrupting oscillator homogeneity in space makes the system lose synchrony earlier in time  
299 (Fig. 6a). This acceleration is quantified in terms of the transition starting time  $\tau_0$ .  $\tau_0$  is greatly reduced  
300 by introducing multiple nuclei in the system (115 min, +XS), driving the system with CSF extract from  
301 the boundary (146 min, +CSF), or combining both of them (45 min, +XS/+CSF), compared to the control  
302 experiment (462 min, Control). The transition rate is also affected substantially by heterogeneity, particularly  
303 by nuclei (Fig. 6b). The slowdown of wave speed after  $\tau_0$  that approaches the terminal trigger wave speed is

304 well characterized by an exponential decay with a time scale  $\Delta\tau$  that varies across experimental conditions.  
305  $\Delta\tau$  is much shorter for extracts with nuclei (157 min for +XS and 83 min for +XS/+CSF) as opposed to  
306 cytoplasm-only experiments (411 min for +CSF and 528 min for Control), which signifies the important  
307 role of having multiple pacemakers in the entrainment.

308 Interestingly, despite the spatial heterogeneity may cause one-order-of-magnitude changes both in  $\tau_0$  and  
309  $\Delta\tau$ , the terminal speed across all conditions remains mostly unchanged (Fig. 6c). This suggests that regardless  
310 of the specific mechanism that drives the transition, coupled mitotic oscillators eventually synchronize with a  
311 consistent timing gradient established by trigger waves of 30-40  $\mu\text{m}/\text{min}$  speed. A recent work by Huang  
312 *et al.* also highlighted the robustness of mitotic trigger wave speed under the physical stress of changing  
313 cytoplasmic concentrations<sup>32</sup>. Such a particular feature of being a reliable reference of timing distinguishes  
314 trigger waves from phase waves. In the absence of dynamic constraints imposed by diffusion, phase waves  
315 propagate at a fast but arbitrary speed that may depend on different physiological circumstances individual  
316 cells face. The speed of trigger waves, on the other hand, is a more intrinsic property of a dynamical system  
317 as explored in our theoretical work (Fig. 5).

## DISCUSSION

318 Spatial coordination is essential to communicating complex biological processes. In this work, we probed  
319 the nature of one such coordination mechanism: mitotic waves that coordinate the process of cell division  
320 in large cells. Using a frog egg extract system which reproduces cell cycles *in vitro*, we characterized how  
321 mitosis spreads through the *Xenopus laevis* cytoplasm via either phase waves or trigger waves.

322 Although properties of trigger waves have been thoroughly studied in the literature<sup>21,22,33-37</sup>, the prop-  
323 erties of their transient dynamics have not. Through our frog egg extract experiments in thin long (quasi-  
324 one-dimensional) tubes, we observed phase waves in the transient dynamics towards the formation of a  
325 stable trigger wave. Even though cell cycle oscillations also slowed down, we showed that this is not  
326 required to observe a transition from phase waves to trigger waves. Certainly, it can take a long time before  
327 a pacemaker—a region that oscillates faster than its surroundings—is able to entrain its surroundings via  
328 trigger waves<sup>21,22</sup>. While in excitable media, a trigger wave can travel uninterrupted throughout the medium,  
329 in oscillatory media the entrainment distance is limited by the inherent oscillatory period of its surroundings.  
330 Even in the transient time when a trigger wave is still forming, the regular biochemical oscillations that drive  
331 the early embryonic cell cycle in *Xenopus laevis* will drive the whole system into mitosis throughout the

332 whole medium. Any phase gradients will thus give rise to phase waves as the cell cycle phase is swept up.

333 This puts our work in dialogue with the existing literature regarding mitotic waves in *Drosophila*.  
334 Although period lengthening was found to be a driver of a sweep-to-trigger transition in *Drosophila*<sup>17</sup>, we  
335 showed that this is not required for directing a transition from phase waves to trigger waves. Furthermore, this  
336 and other work highlight that phase wave properties are not robust to heterogeneity as they do not correspond  
337 to an actual attracting system solution. In Hayden *et al.*<sup>17</sup>, the authors also show embryos displaying a  
338 nuclear density gradient in the syncytial embryo can lead to trigger rather than sweep or phase waves. We  
339 demonstrate a similar effect of disrupting homogeneity both by adding nuclei to the homogeneous system  
340 and by driving it explicitly with CSF. In all three cases, these trigger-wave-producing effects overtake the  
341 underlying quasi-synchronous patterns.

342 As phase waves do not actively propagate through a medium and require structured initial phase differ-  
343 ences over a certain distance, they typically only persist for hundreds of micrometers. A trigger wave can  
344 travel long distances ( $\sim 10$  mm), and the typical length scale of the concentration gradient at the leading front  
345 ranges around hundreds of microns as well. This underscores the prevalence of phase waves in relatively  
346 small embryos, such as *Drosophila*, due to the limited length to accommodate a trigger wave front gradient.  
347 On the scale of some biological functions, the propagation distance of phase waves is relevant. However,  
348 for the specific purpose of coordination, this proves insufficient in larger cells. Trigger waves, as made  
349 evident by our work here, conversely, transmit signals orders of magnitude farther in distance. This questions  
350 the physiological relevance of phase waves. At most, one could argue for a tradeoff between speed and  
351 distance. For mitosis it could be reasonable that nature would select for trigger waves in larger embryos such  
352 as *Xenopus*, where coordinating over large distances is more relevant than in *Drosophila*. Recently reported  
353 ultrafast waves<sup>10,16,38,39</sup>, faster-than-trigger-wave signaling achieved without requiring bistable reactions or  
354 diffusion-mediated coupling, necessitate further comprehensive studies to understand the fundamental nature  
355 of these waves in comparison to classical trigger waves. Our work highlights the importance of examining  
356 not only stable waves but also the time evolution of waves as they develop. It also provides a framework that  
357 integrates experiments and theory to dissect the transition between different wave regimes.

358 Future experiments could expand on this work by pursuing other forms of perturbations by inhibiting the  
359 feedback loops in the network. The field already demonstrated the importance of Wee1 for “forming the  
360 trigger”<sup>8</sup>, but with our setup and analysis framework, one could quantify the effect and provide stronger  
361 evidence in either direction. The same applies to Cdc25, a phosphatase acting antagonistically to the Wee1

362 kinase in the regulation of Cdk1, both forming positive feedback loops with Cdk1. It would be interesting  
363 to observe whether Wee1 and Cdc25 affect this time dependence in similar manners. Moreover, we know  
364 that these inputs also translocate in and out of the nucleus throughout one cycle, at different times<sup>40,41</sup>. It  
365 stands to reason that inhibition thereof could change in the presence of nuclei, and thus, we might see a  
366 nuclei-dependent effect on how inhibition perturbs this transition. Clearly, much work remains on elucidating  
367 the details of time-dependent wave behavior.

368 In another vein, the CSF driving setup could be used to expand on this study by asking how perturbations  
369 to the clock network, including inhibitions for other clock constituents such as Cdc25, Wee1, PP2A, etc.,  
370 change trigger wave propagation. Furthermore, like CSF extracts, interphase extracts maintain activity for  
371 months while frozen, making them more accessible for faster and simpler data acquisition than involving  
372 the cycling system. In practice, such experiments could provide a more straightforward method for testing  
373 all of the perturbations mentioned above: clock inhibitors, glycerol-modulated diffusion, etc. In particular,  
374 this would facilitate a direct examination of whether nuclei indeed perturb wave propagation as it would  
375 eliminate their dual role as a pacemaker. In total, this setup offers a wealth of opportunities to probe trigger  
376 wave dynamics, relevant for *in vivo* embryogenesis in *Xenopus*.

377 Moreover, one can envision perturbing the source itself. Theory predicts the wave speed to depend  
378 on the difference between the pacemaker and bulk frequency<sup>21,22</sup>. Modulating the driving force of the  
379 CSF source, whether through dilution or the use of inhibitors, can provide a direct test of these theoretical  
380 predictions. As the interplay between CSF arrest and its driving force remains unclear, comprehending such  
381 perturbations requires additional modeling efforts. Nevertheless, our successful demonstration of driving  
382 waves *in vitro* underscores the significance of elucidating these interactions. Taken together, these future  
383 investigations would not only enhance our understanding of how organisms transmit mitotic information  
384 across long distances, but also provide fundamental insights into the nature of biochemical waves generally,  
385 and phase waves and trigger waves in particular.

## METHODS

### *Xenopus laevis* egg extracts

386 To capture mitotic waves *in vitro*, we made cell-free cycling extracts from *Xenopus laevis* eggs following a  
387 published protocol<sup>18,19</sup> adapted from Murray<sup>26</sup>. Extracts were then supplemented with various reporters,  
388 drugs and/or sperm DNA, depending on the experimental conditions. The Cdk1-FRET sensor was prepared

389 as described in Maryu and Yang<sup>15</sup>. Demembrated sperm DNA was prepared following the established  
390 protocol<sup>26</sup>. Work from the Yang lab demonstrated an intermediate range of dilution of the extracts can  
391 improve the number of cycles, with the best activity at around 20% dilution<sup>42</sup>. As a result, for the data  
392 described here, the dilution was kept constant at 20% with extract buffer (100 mM KCl, 0.1 mM CaCl<sub>2</sub>,  
393 1 mM MgCl<sub>2</sub>, 10 mM potassium HEPES, 50 nM sucrose, pH 7.8). Extracts were subsequently loaded into  
394 5-10 mm-long sections of Teflon-coated Masterflex PTFE tubing (inner diameter 150 μm) via aspiration,  
395 submerged under mineral oil, and then recorded using time-lapse epifluorescent microscopy (Olympus  
396 IX-83). Given the dimensions of the tubing used, tubes were organized into, at most, groups of five in one  
397 direction. We did not observe any significant contamination between tubes, even when forcing them into  
398 such close proximity.

399 For Figs. 4b and 4c, frozen interphase extracts were made using the standard protocol in the field<sup>20,31</sup>.  
400 On the day of the experiment, one aliquot is thawed on ice, supplemented with reporters, and then loaded  
401 into PTFE tubing for imaging.

402 The CSF extracts were made following established protocols<sup>29</sup> adapted from the original<sup>26</sup>. Using laid  
403 eggs, we produced large quantities of extract (on the order of mL), vastly more than necessary for a single  
404 experiment (10-20 μL). To preserve said large quantities of extract, we implemented a freezing protocol  
405 adopted from Takagi and Shimamoto<sup>30</sup>. To maintain conditions across the reservoir and the cycling extract,  
406 CSF extracts were also diluted to 20% with extract buffer. No reporters or drugs were added to these extracts.

407 In order to set up the CSF driven system, we first cut PTFE tubing into individual sections of ~ 10 mm  
408 lengths and loaded each via aspiration such that the extract (either interphase or cycling extracts) filled the  
409 tube in excess: visual inspection of the syringe adapter showed the fluid line exceeding the tube opening.  
410 Then the tube was dipped into the CSF reservoir syringe-end first for 5-10 seconds to ensure fluidic contact  
411 between the cycling/interphase and CSF extracts. While the original apoptotic wave paper<sup>24</sup> described  
412 maintaining contact between the reservoir and tubes for many minutes, we observed any contact longer than  
413 ~ 10 seconds resulted in mitotic arrest overtaking most, if not all, of the tube. This sometimes occurred even  
414 at shorter dipping times. As such, care was taken to minimize the contact time. Tubes were then submerged  
415 under mineral oil and imaged as discussed above.

## Image processing and analysis methods

416 Grids of images were captured and subsequently stitched together using ImageJ's Grid/Pairwise Stitching  
417 plug-in<sup>43</sup>, in conjunction with additional pipeline code written in Fiji/Java. Bright-field images from the

418 first frame were used to generate stitching parameters, which were fed to ImageJ to stitch each channel  
419 at each frame consecutively. While capturing grids of images in this way resulted in a non-zero time lag  
420 between subsequent sections along a tube, and multiple of this lag between the first and last sections, this  
421 gap amounted to a few seconds, much smaller than the scale of the overall imaging timestep which was  
422 on the order of minutes. As such, this was ignored for the purposes of analysis. The stitched stacks were  
423 then straightened using Fiji and a manually selected curve from the bright-field images as an input. This  
424 curve was unique to each tube, though the profiles of the tubing sections often followed roughly the same  
425 shape, with not much distortion. Afterwards, the tube images were cropped so as to only include the inner  
426 dimension, again using the bright-field images as a guide. Additionally, the FRET ratio was calculated  
427 separately as in Maryu and Yang<sup>15</sup>.

428 For the analysis of wavefronts, first, individual kymographs were corrected for any decaying baseline  
429 trend, and any NaN pixels were filled using the scikit-image function `inpaint`. Afterwards, we detected  
430 peaks for each time series at each pixel along the tube. The peaks themselves were then clustered into  
431 individual cycles in Python. Once cycles were identified and separated, the collection(s) of peaks were fitted  
432 and/or smoothed in space and time, after which slopes (and speeds) were calculated along each front by  
433 taking the numerical derivative of the fits at each point. Periods followed directly from the detected peaks.  
434 The normalized density estimation for the time dependence of the period, slope, and maximum activation  
435 rate made use of the SciPy function `scipy.stats.gaussian_kde` using a Gaussian kernel of  $\sigma_t = 50$  min  
436 as a sliding window for time and the maximum value normalized to one.

## Moving horizon fitting

437 To determine  $\tau_0$ , we examined the quality of the exponential fitting of the wave speed's later-time decay, by  
438 calculating mean square residual (MSR) of the fitting for the time frame  $[\tau_0, \infty)$ . Both the MSR (Fig. S1,  
439 top) and its derivative with respect to  $\tau$  (Fig. S1, bottom) sharply changed (Control, +XS, and +CSF) at a  
440 finite  $\tau$  indicating the fitting at the tail segment abruptly worsened upon extending it to earlier times.  $\tau_0$  was  
441 defined as the largest time that the derivative lies below a chosen threshold,  $-0.025 \mu\text{m}^2/\text{min}^3$  (horizontal  
442 red line).  $\tau_0$  was affected minimally by the choice of the threshold due to the sharp change in the derivative.  
443 This definition applied consistently across data with varying fitting quality (for example, +XS data has an  
444 overall lower fitting quality than +XS/+CSF data), making it preferable over other thresholding methods  
445 based solely on MSR. If the fitting quality is good for all scanned  $\tau$  values (in the case of +XS/+CSF), the  
446 earliest recorded time was defined as  $\tau_0$ .

## Mathematical model

447 We use the mathematical model previously introduced<sup>8,20</sup> describing the dynamics of the total cyclin B-Cdk1  
 448  $c \equiv c(x, t)$  and its active form  $a \equiv a(x, t)$ . The equations can be written in the following form:

$$\partial_t c = \eta \beta (k_s - h_{\text{Deg}}(a)c) + D \nabla^2 c, \quad (1)$$

$$\partial_t a = \eta [\alpha (h_{\text{Cdc25}}(a)(c - a) - h_{\text{Wee1}}(a)a) + \beta (k_s - h_{\text{Deg}}(a)a)] + D \nabla^2 a, \quad (2)$$

449 where the newly introduced dimensionless parameters are  $\alpha$ ,  $\beta$ , and  $\eta$ . The parameter  $\eta$  scales all parameter  
 450 rates and allows for precise control of the period of the oscillations. The parameter  $\alpha$  scales the rates related  
 451 to activation-inactivation processes mediated by Cdc25 phosphatase and Wee1 kinase, which are described  
 452 by Hill functions of the form

$$h_{\text{Cdc25}}(a) = a_{\text{Cdc25}} + \frac{b_{\text{Cdc25}} a^{n_{\text{Cdc25}}}}{\text{EC}_{50, \text{Cdc25}}^{n_{\text{Cdc25}}} + a^{n_{\text{Cdc25}}}}, \quad (3)$$

$$h_{\text{Wee1}}(a) = a_{\text{Wee1}} + \frac{b_{\text{Wee1}} \text{EC}_{50, \text{Wee1}}^{n_{\text{Wee1}}}}{\text{EC}_{50, \text{Wee1}}^{n_{\text{Wee1}}} + a^{n_{\text{Wee1}}}}. \quad (4)$$

453 The parameter  $\beta$  scales synthesis and degradation rates to control the time spent in interphase and mitosis.  
 454 The degradation term encompasses the APC/C-induced degradation of cyclin B which is described with the  
 455 hill function

$$h_{\text{Deg}}(a) = a_{\text{Deg}} + \frac{b_{\text{Deg}} a^{n_{\text{Deg}}}}{\text{EC}_{50, \text{Deg}}^{n_{\text{Deg}}} + a^{n_{\text{Deg}}}}. \quad (5)$$

456 The parameters of the model are  $k_s = 1.5$  nM/min,  $a_{\text{Cdc25}} = 0.8$  min<sup>-1</sup>,  $b_{\text{Cdc25}} = 4$  min<sup>-1</sup>,  $\text{EC}_{50, \text{Cdc25}} =$   
 457  $35$  nM,  $n_{\text{Cdc25}} = 11$ ,  $a_{\text{Wee1}} = 0.4$  min<sup>-1</sup>,  $b_{\text{Wee1}} = 2$  min<sup>-1</sup>,  $\text{EC}_{50, \text{Wee1}} = 30$  nM,  $n_{\text{Wee1}} = 3.5$ ,  $a_{\text{Deg}} =$   
 458  $0.01$  min<sup>-1</sup>,  $b_{\text{Deg}} = 0.06$  min<sup>-1</sup>,  $\text{EC}_{50, \text{Deg}} = 32$  nM,  $n_{\text{Deg}} = 17$ ,  $\alpha = \beta = \eta = 1$  and are kept constant  
 459 in this work otherwise specified.

## Numerical simulations

460 The model described by Eqs. (1) and (2) is a system of two coupled partial differential equations integrated  
 461 in time with a pseudo-spectral method<sup>44</sup>. We consider a grid with  $N_x$  grid points to describe a spatial domain  
 462 of length  $L_x$  with no-flux boundary conditions and we integrate with a timestep  $\Delta t$  the linear terms in Fourier  
 463 space exactly, while the nonlinear terms are integrated using a second-order in time approximation.

464 Numerical simulations showing the transition from phase to trigger waves in time (Figs. 2b, 2c, 2d, and

465 **2e)** have been performed using the integration parameters  $N_x = 4096$ ,  $L_x = 10$  mm, and  $\Delta t = 0.002$  min  
 466 starting with an initial condition of  $a(x) = c(x) = 0$  nM introducing spatial heterogeneity in the synthesis  
 467 term of the following form:  $k_s(x) = k_s[1 + \Theta(x) + A_k N(x)]$ , where  $\Theta(x)$  is a manually introduced profile to  
 468 induce pacemakers at chosen locations for visualization porpoises and set to zero in Fig. 2c to explore the  
 469 impact of the synthesis noise amplitude  $A_k$ . The introduced heterogeneity  $N(x)$  is computed by generating  
 470 colored noise  $n(x) = F^{-1}[\exp(-(\sigma k)^2/2 - 2i\pi u_k)](x)$  using the inverse Fourier transform  $F^{-1}$  where  $u_k$  is  
 471 a random number uniformly distributed between 0 and 1 for each Fourier mode  $k$  and the typical length scale  
 472 of the spatial heterogeneities is chosen  $\sigma = 77.46$   $\mu\text{m}$ . The noise is later normalized to have a maximum  
 473 value of one with the expression,

$$N(x) = \frac{n(x) - \int_0^{L_x} n(x) dx / L_x}{\max[n(x) - \int_0^{L_x} n(x) dx / L_x]}. \quad (6)$$

474 The temporal dependence  $\beta(t)$  is computed using the linear dependence of the period  $T(1/\beta)$  shown  
 475 in Fig. 2a (middle) to reproduce the experimentally observed time-dependence of the period in Fig. 1d  
 476 (top). The calculated  $\beta(t)$  is initialized at the time of the second oscillation, which corresponds to the first  
 477 measurement of the period in the experiments.

478 Numerical simulations in Fig. 5 have been performed using the integration parameters  $N_x = 1024$ ,  
 479  $L_x = 5$  mm, and  $\Delta t = 0.002$  min starting with an initial condition  $a(x) = c(x) = 0$  and introducing a  
 480 pacemaker at the center using a step function as  $\Theta(x) = \Delta\Theta H(s/2 - |x - L_x/2|)$  where  $\Delta\Theta = 0.3$ ,  $H(x)$  is  
 481 the Heaviside function, and  $s = 50$   $\mu\text{m}$  for simulations showing trigger waves. Simulations showing phase  
 482 waves use a constant value of  $\Theta(x)$  and as initial condition for  $a(x) = 2(a_{\min} - a_{\max})|x - L_x/2|/L_x + a_{\min}$  a  
 483 linear triangular spatial profile of decreasing activity from  $a_{\max} = 20$  to  $a_{\min} = 0$  nM as the distance from  
 484 the center increases.

## CODE AVAILABILITY

485 Python codes for the analysis of mitotic waves properties and Fortran codes for performing numerical  
 486 simulations are deposited on GitHub. Codes are available from Zenodo:

487 <https://zenodo.org/doi/10.5281/zenodo.10583185><sup>45</sup> and from Gelens Lab GitLab

488 [https://gitlab.kuleuven.be/gelenslab/publications/mitotic\\_waves](https://gitlab.kuleuven.be/gelenslab/publications/mitotic_waves).

## ACKNOWLEDGEMENTS

489 Q.Y. acknowledges funding from the National Science Foundation (MCB#2218083) and the National  
490 Institutes of Health (R01GM144584). L.G. acknowledges funding from the Research Foundation Flanders  
491 (FWO, grant number G074321N). D.R.-R. is supported by the Ministry of Universities through the “Pla de  
492 Recuperació, Transformació i Resilència” and by the EU (NextGenerationEU), together with the Universitat  
493 de les Illes Balears.

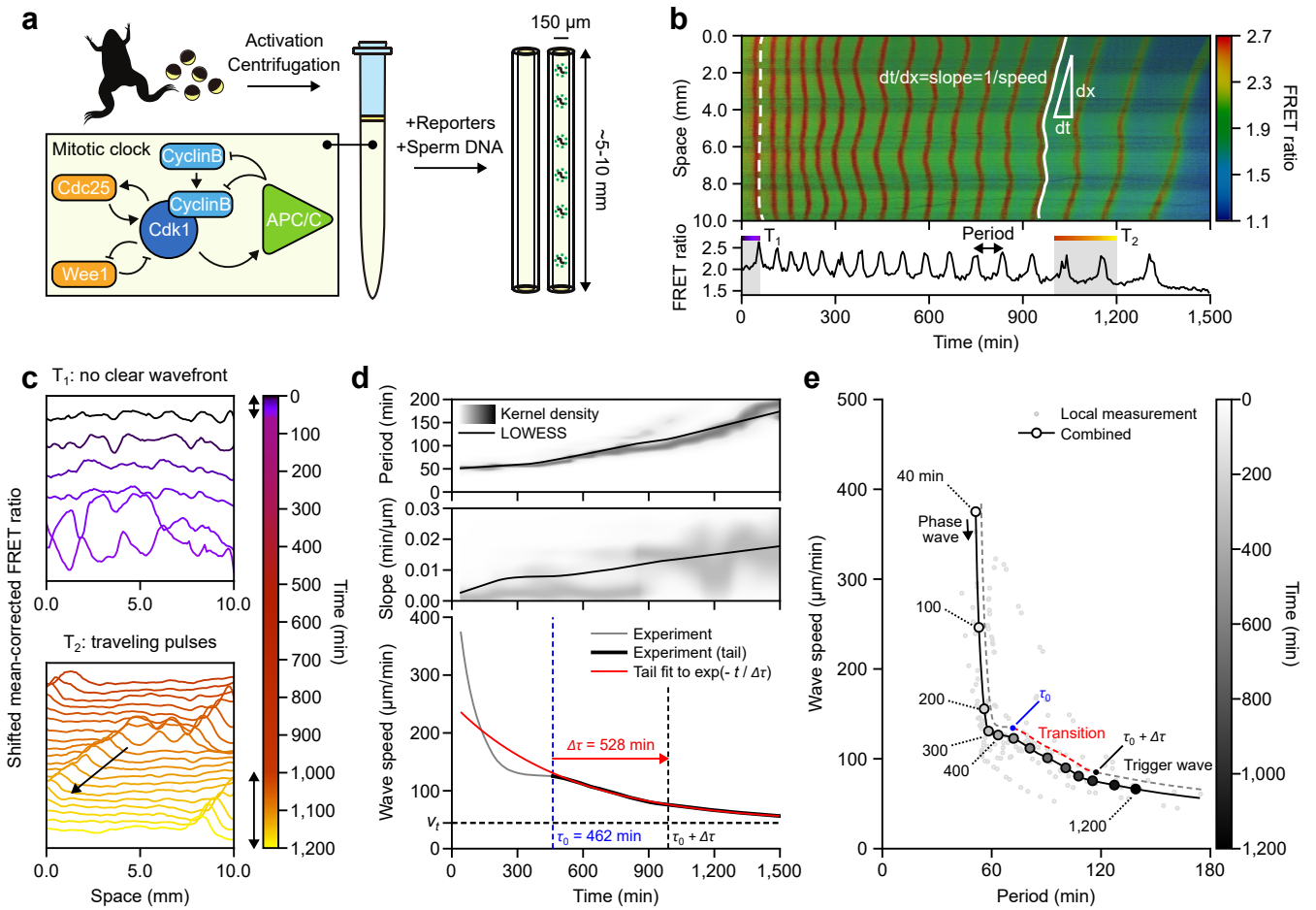
## REFERENCES

- 494 1. Novak, B. & Tyson, J. J. Numerical analysis of a comprehensive model of M-phase control in *Xenopus*  
495 oocyte extracts and intact embryos. *J. Cell. Sci.* **106**, 1153–1168 (1993).
- 496 2. Novak, B. & Tyson, J. J. Modeling the cell division cycle: M-phase trigger, oscillations, and size control.  
497 *J. Theor. Biol.* **165**, 101–134 (1993).
- 498 3. Morgan, D. O. *The Cell Cycle: Principles of Control* (New Science Press, 2007).
- 499 4. Foe, V. E. & Alberts, B. M. Studies of nuclear and cytoplasmic behaviour during the five mitotic cycles  
500 that precede gastrulation in *Drosophila* embryogenesis. *J. Cell. Sci.* **61**, 31–70 (1983).
- 501 5. Hara, K., Tydeman, P. & Kirschner, M. A cytoplasmic clock with the same period as the division cycle  
502 in *Xenopus* eggs. *Proc. Natl. Acad. Sci.* **77**, 462–466 (1980).
- 503 6. Farrell, J. A. & O’Farrell, P. H. From egg to gastrula: how the cell cycle is remodeled during the  
504 *Drosophila* mid-blastula transition. *Annu. Rev. Genet.* **48**, 269–294 (2014).
- 505 7. Anderson, G. A., Gelens, L., Baker, J. C. & Ferrell, J. E. Desynchronizing embryonic cell division  
506 waves reveals the robustness of *Xenopus laevis* development. *Cell. Rep.* **21**, 37–46 (2017).
- 507 8. Chang, J. B. & Ferrell Jr, J. E. Mitotic trigger waves and the spatial coordination of the *Xenopus* cell  
508 cycle. *Nature* **500**, 603–607 (2013).
- 509 9. Deneke, V. E., Melbinger, A., Vergassola, M. & Di Talia, S. Waves of cdk1 activity in s phase synchronize  
510 the cell cycle in *Drosophila* embryos. *Dev. Cell.* **38**, 399–412 (2016).
- 511 10. Deneke, V. E. & Di Talia, S. Chemical waves in cell and developmental biology. *J. Cell. Biol.* **217**,  
512 1193–1204 (2018).
- 513 11. Gelens, L., Anderson, G. A. & Ferrell Jr, J. E. Spatial trigger waves: positive feedback gets you a long  
514 way. *Mol. Biol. Cell.* **25**, 3486–3493 (2014).
- 515 12. Di Talia, S. & Vergassola, M. Waves in embryonic development. *Annu. Rev. Biophys.* **51**, 327–353  
516 (2022).
- 517 13. Nolet, F. E. *et al.* Nuclei determine the spatial origin of mitotic waves. *eLife* **9**, e52868 (2020).
- 518 14. Afanзар, O., Buss, G. K., Stearns, T. & Ferrell Jr, J. E. The nucleus serves as the pacemaker for the cell  
519 cycle. *eLife* **9**, e59989 (2020).
- 520 15. Maryu, G. & Yang, Q. Nuclear-cytoplasmic compartmentalization of cyclin b1-cdk1 promotes robust  
521 timing of mitotic events. *Cell. Rep.* **41** (2022).
- 522 16. Vergassola, M., Deneke, V. E. & Di Talia, S. Mitotic waves in the early embryogenesis of *Drosophila*:

- 523 Bistability traded for speed. *Proc. Natl. Acad. Sci.* **115**, E2165–E2174 (2018).
- 524 17. Hayden, L., Hur, W., Vergassola, M. & Di Talia, S. Manipulating the nature of embryonic mitotic waves.  
525 *Curr. Biol.* **32**, 4989–4996 (2022).
- 526 18. Guan, Y. *et al.* A robust and tunable mitotic oscillator in artificial cells. *eLife* **7**, e33549 (2018).
- 527 19. Guan, Y., Wang, S., Jin, M., Xu, H. & Yang, Q. Reconstitution of cell-cycle oscillations in microemul-  
528 sions of cell-free *Xenopus* egg extracts. *J. Vis. Exp.* e58240 (2018).
- 529 20. Yang, Q. & Ferrell Jr, J. E. The cdk1–apc/c cell cycle oscillator circuit functions as a time-delayed,  
530 ultrasensitive switch. *Nat. Cell. Biol.* **15**, 519–525 (2013).
- 531 21. Rombouts, J. & Gelens, L. Synchronizing an oscillatory medium: The speed of pacemaker-generated  
532 waves. *Phys. Rev. Res.* **2**, 043038 (2020).
- 533 22. Rombouts, J. & Gelens, L. Analytical approximations for the speed of pacemaker-generated waves.  
534 *Phys. Rev. E.* **104**, 014220 (2021).
- 535 23. Nolet, F. E. & Gelens, L. Mitotic waves in an import-diffusion model with multiple nuclei in a shared  
536 cytoplasm. *Biosystems* **208**, 104478 (2021).
- 537 24. Cheng, X. & Ferrell Jr, J. E. Apoptosis propagates through the cytoplasm as trigger waves. *Science* **361**,  
538 607–612 (2018).
- 539 25. Masui, Y. & Markert, C. L. Cytoplasmic control of nuclear behavior during meiotic maturation of frog  
540 oocytes. *J. Exp. Zool.* **177**, 129–145 (1971).
- 541 26. Murray, A. W. Cell cycle extracts. *Methods Cell. Biol.* **36**, 581–605 (1991).
- 542 27. Schmidt, A., Rauh, N. R., Nigg, E. A. & Mayer, T. U. Cytostatic factor: an activity that puts the cell  
543 cycle on hold. *J. Cell. Sci.* **119**, 1213–1218 (2006).
- 544 28. Yamamoto, T. M., Iwabuchi, M., Ohsumi, K. & Kishimoto, T. Apc/c–cdc20-mediated degradation of  
545 cyclin b participates in csf arrest in unfertilized *Xenopus* eggs. *Dev. Biol.* **279**, 345–355 (2005).
- 546 29. Good, M. C. & Heald, R. Preparation of cellular extracts from *Xenopus* eggs and embryos. *Cold Spring*  
547 *Harb. Protoc.* (2018).
- 548 30. Takagi, J. & Shimamoto, Y. High-quality frozen extracts of *Xenopus laevis* eggs reveal size-dependent  
549 control of metaphase spindle micromechanics. *Mol. Biol. Cell.* **28**, 2170–2177 (2017).
- 550 31. Deming, P. & Kornbluth, S. Study of apoptosis *in vitro* using the *Xenopus* egg extract reconstitution  
551 system. *Xenopus Protoc. Cell. Biol. Signal Transduct.* 379–393 (2006).
- 552 32. Huang, J.-H., Chen, Y., Huang, W. Y., Tabatabaee, S. & Ferrell Jr, J. E. Robust trigger wave speed in

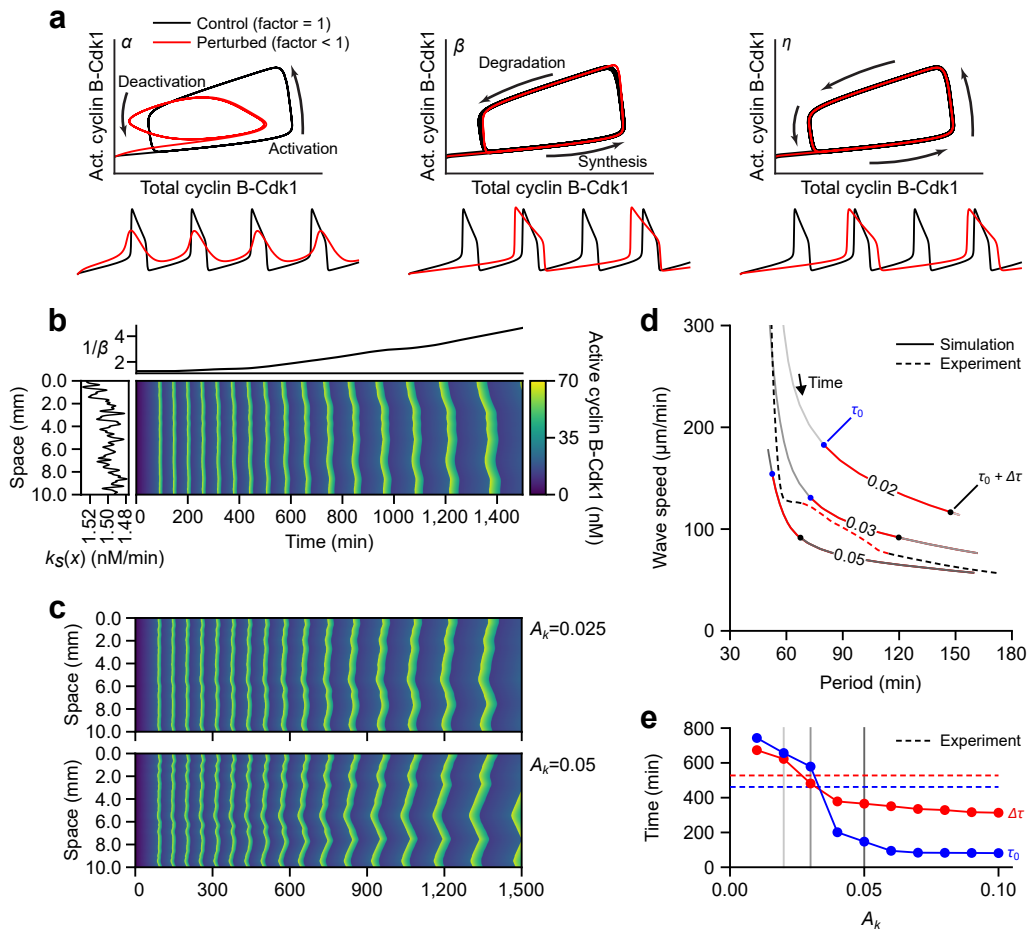
- 553 *Xenopus* cytoplasmic extracts. *bioRxiv* 2023–12 (2023).
- 554 33. Tyson, J. J. & Keener, J. P. Singular perturbation theory of traveling waves in excitable media (a review).  
555 *Phys. D: Nonlinear Phenom.* **32**, 327–361 (1988).
- 556 34. Elphick, C., Hagberg, A., Malomed, B. & Meron, E. On the origin of traveling pulses in bistable systems.  
557 *Phys. Lett. A* **230**, 33–37 (1997).
- 558 35. Hagberg, A. & Meron, E. Pattern formation in non-gradient reaction-diffusion systems: the effects of  
559 front bifurcations. *Nonlinearity* **7**, 805 (1994).
- 560 36. Rinzel, J. & Terman, D. Propagation phenomena in a bistable reaction-diffusion system. *SIAM J. on*  
561 *Appl. Math.* **42**, 1111–1137 (1982).
- 562 37. Bode, M. Front-bifurcations in reaction-diffusion systems with inhomogeneous parameter distributions.  
563 *Phys. D: Nonlinear Phenom.* **106**, 270–286 (1997).
- 564 38. Puls, O. & Yang, Q. The rise of ultrafast waves. *Dev. Cell.* **47**, 532–534 (2018).
- 565 39. Wu, Z., Su, M., Tong, C., Wu, M. & Liu, J. Membrane shape-mediated wave propagation of cortical  
566 protein dynamics. *Nat. Commun.* **9**, 136 (2018).
- 567 40. Baldin, V. & Ducommun, B. Subcellular localisation of human wee1 kinase is regulated during the cell  
568 cycle. *J. Cell. Sci.* **108**, 2425–2432 (1995).
- 569 41. Trunnell, N. B., Poon, A. C., Kim, S. Y. & Ferrell, J. E. Ultrasensitivity in the regulation of cdc25c by  
570 cdk1. *Mol. Cell.* **41**, 263–274 (2011).
- 571 42. Jin, M., Tavella, F., Wang, S. & Yang, Q. *In vitro* cell cycle oscillations exhibit a robust and hysteretic  
572 response to changes in cytoplasmic density. *Proc. Natl. Acad. Sci.* **119**, e2109547119 (2022).
- 573 43. Preibisch, S., Saalfeld, S. & Tomancak, P. Globally optimal stitching of tiled 3d microscopic image  
574 acquisitions. *Bioinformatics* **25**, 1463–1465 (2009).
- 575 44. Montagne, R., Hernández-García, E., Amengual, A. & San Miguel, M. Wound-up phase turbulence in  
576 the complex ginzburg-landau equation. *Phys. Rev. E.* **56**, 151 (1997).
- 577 45. Puls, O. *et al.* Speeding up phase-to-trigger wave transitions: the role of spatial heterogeneity revealed  
578 in frog egg extracts. <https://zenodo.org/doi/10.5281/zenodo.10583185> (2024).

## FIGURES AND FIGURE LEGENDS

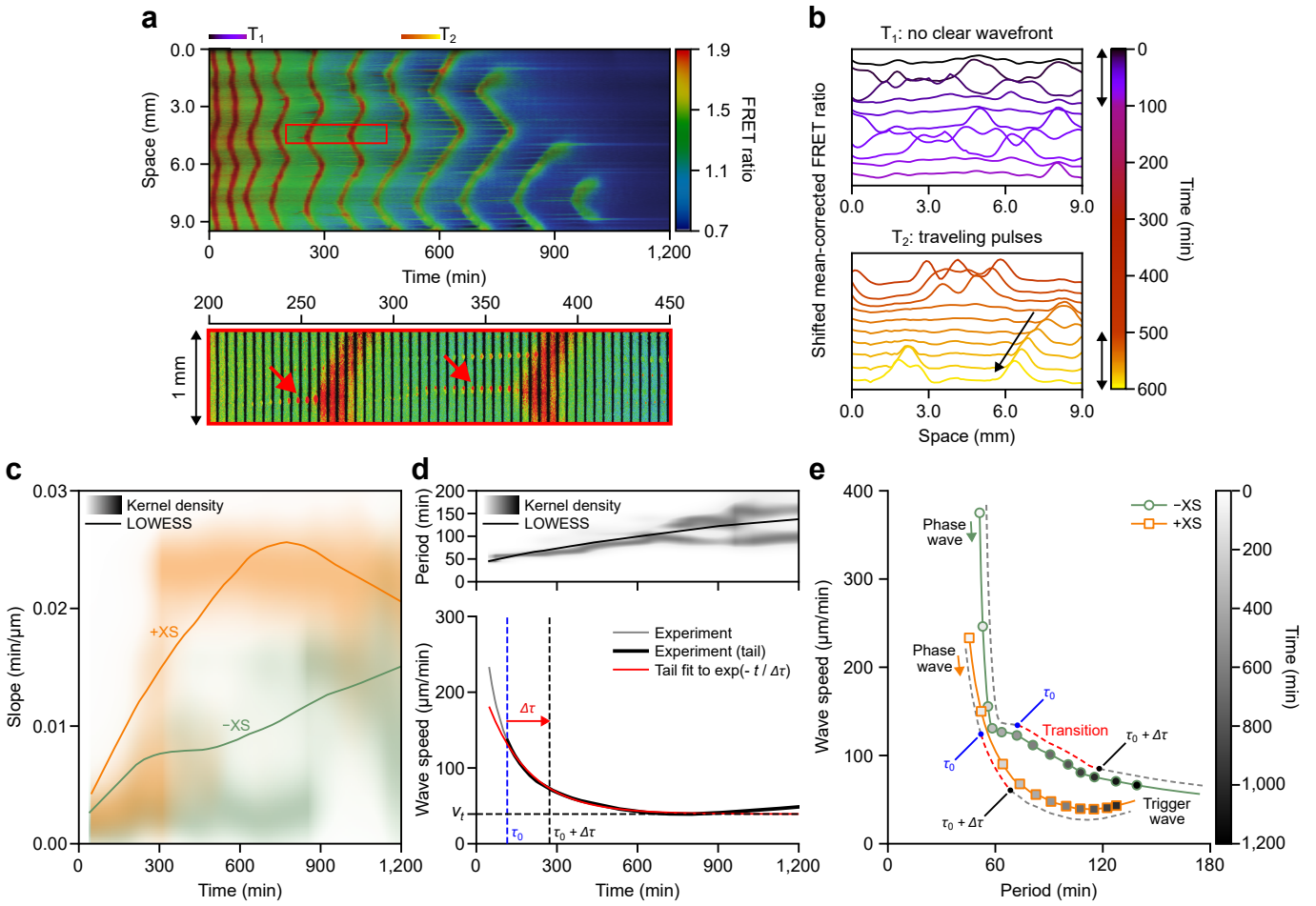


579 **Fig. 1 Time evolution of mitotic waves.** **a** Schematic view of the experimental preparation of cycling  
 580 egg extracts of *Xenopus laevis* supplied with Cdk1-FRET sensor, as a reporter, and loaded in Teflon tubes  
 581 of  $\sim 5$ -10 mm long and 150  $\mu\text{m}$  of inner diameter. Before loading, extracts were added with *Xenopus*  
 582 demembrated sperm DNA (+XS) or without (−XS, Control). Bottom-Left: Schematic representation of  
 583 the regulatory network driving the mitotic oscillations. **b** Top: FRET ratio kymograph for a representative  
 584 tube of 10 mm long loaded with extracts without sperm DNA (−XS). The top end of the tube is assigned  
 585 to  $x = 10$  mm. Color bar indicates FRET ratio values. For illustration purposes, two detected wavefronts  
 586 are labeled in white lines (dashed for a wave at an early time and solid for a later-time wave). The slope  
 587 ( $dt/dx$ ) of these wavefronts describes the change in time with respect to traveling distance and is the inverse  
 588 of speed. Bottom: FRET ratio time course recorded at the bottom end of the Teflon tube ( $x = 10$  mm). The  
 589 period is defined as the time interval between consecutive FRET ratio peaks. One early time region,  $T_1$ ,  
 590 and one late time region,  $T_2$ , are selected for further analysis in panel **c**. **c** Shifted mean-corrected FRET  
 591 signal for two different time regions,  $T_1$  and  $T_2$ , defined in B across the Teflon tube. Top: Early-time signal

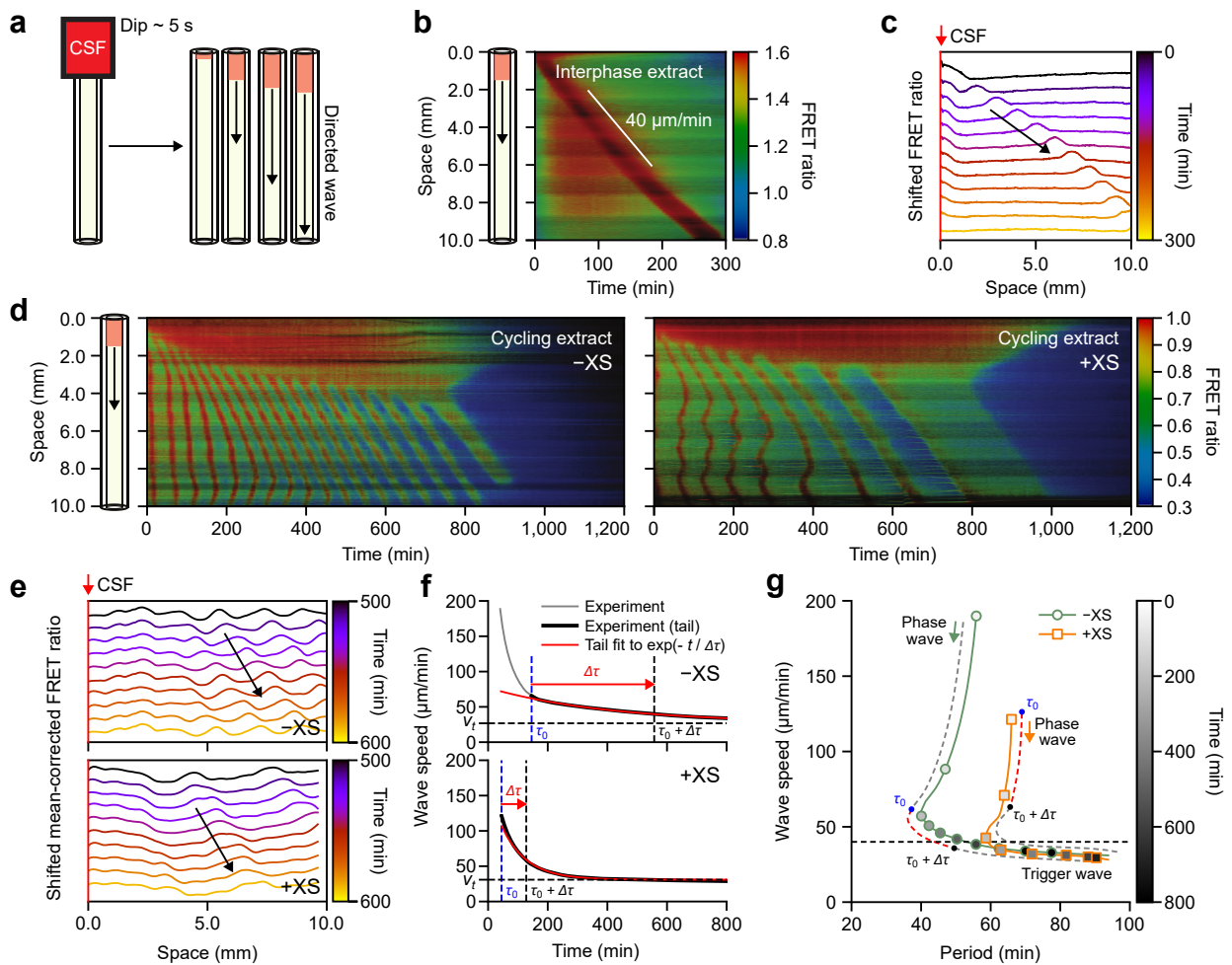
592 showing in-phase activation with no clear wavefront. Bottom: Late-time signal showing a traveling pulse  
593 crossing the tube over time, as indicated by the black arrow. Bidirectional arrows on the colorbar indicate  $T_1$   
594 and  $T_2$  time regions. **d** Time evolution of the period (top), slope (middle), and wave speed (bottom). Both  
595 period and slope are measured locally for each wavefront locus. Their distributions are represented using the  
596 kernel density estimation (KDE), indicated with a grayscale colormap, and normalized at each time. Period  
597 and slope data are smoothed by locally weighted scatterplot smoothing (LOWESS) and their curves are  
598 shown with solid black lines. The wave speed is obtained as the inverse of the LOWESS estimation of the  
599 slope. The time point at which exponential decay begins ( $\tau_0$ , dashed blue line) is calculated via a moving  
600 horizon fitting (See Methods and Fig. S1 for the definition). The evolution of the speed after  $\tau_0$  is fitted by an  
601 exponential function (solid red line) to calculate the entrainment time ( $\Delta\tau$ ). The horizontal dashed black line  
602 indicates the resulting terminal velocity from the fit ( $v_t$ ) and the vertical dashed black line indicates the time  
603 point corresponding to  $\tau_0 + \Delta\tau$ . **e** Speed-period relationship. Local measurements of the period and wave  
604 speed are represented by gray dots (2% of all data points were shown). Combined speed-period relation  
605 (solid black line) is computed from the LOWESS estimations of the period and speed from **d**. Additional  
606 markers (open circles with grayscale fillings) are placed along this line to indicate multiples of 100 minutes  
607 (except for the first one which is shown for clarity). Grayscale color bar indicates time. The transition time  
608 points  $\tau_0$  and  $\tau_0 + \Delta\tau$  are indicated on a dashed guideline with the transition time frame highlighted in red.  
609 Data in **d** and **e** are pooled from two independent *Xenopus* egg batches and three replicates each.



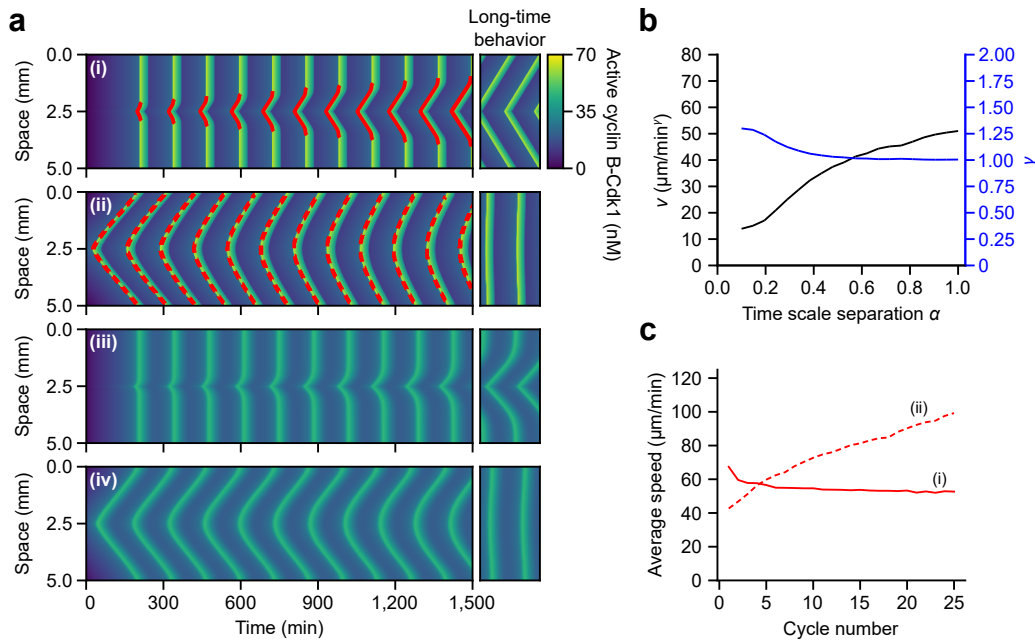
610 **Fig. 2 Mathematical modeling explains the transition from phase to trigger waves.** **a** Schematic  
 611 representation of the mitotic dynamics influenced by scaling factors  $\alpha$  (left),  $\beta$  (middle), and  $\eta$  (right),  
 612 which scale for the rates of respective reactions indicated by black arrows. See Methods and Fig. S3 for  
 613 details. Unperturbed (scaling factor = 1, black lines) and perturbed (scaling factor < 1, red lines) dynamics  
 614 are compared for phase-plane trajectories of total and active cyclin B-Cdk1 concentration (top) and active  
 615 cyclin B-Cdk1 concentration time courses (bottom). **b** Spatiotemporal evolution of the cyclin B-Cdk1  
 616 activity showing the transition from fast to slow waves. Simulation has incorporated the experimental  
 617 time-dependence of the period shown as  $1/\beta(t)$  (top panel) and spatial variability in the synthesis term  $k_s(x)$   
 618 (left panel, see also Methods). **c** Influence of spatial heterogeneity ( $A_k$ ) on the wave speed entrainment.  
 619 **d** Speed-period relation of the experiment (dashed line) and the numerical simulations (solid lines with  
 620 respective  $A_k$  values labeled). The transition points  $\tau_0$  and  $\tau_0 + \Delta\tau$  are marked as in Fig. 1e. The time frames  
 621 between  $\tau_0$  and  $\tau_0 + \Delta\tau$  are highlighted in red. **e** Dependence of transition time scales  $\tau_0$  (blue) and  $\Delta\tau$  (red)  
 622 on spatial heterogeneity. Experimental measurements are given in dashed lines. Vertical lines correspond to  
 623 simulation conditions illustrated in **d** with matching grayscale colors.



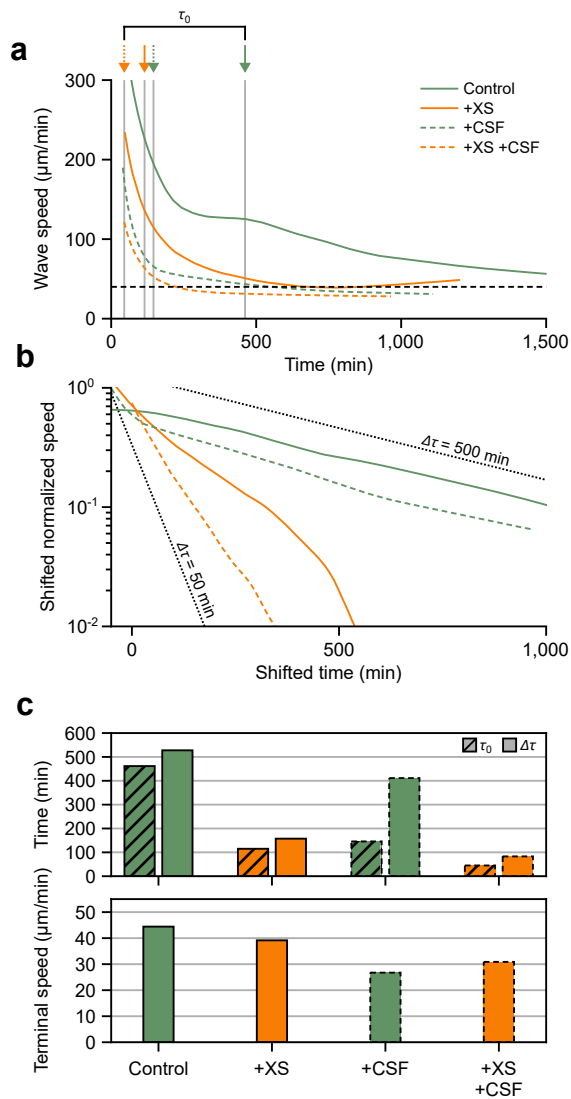
624 **Fig. 3 Nuclei entrain the system to the trigger wave regime.** **a** Representative kymograph of the effects of  
 625 adding sperm DNA (+XS). A magnified view of the region inside the red rectangle is provided in the lower  
 626 panel to show nuclear growth before the entry into mitosis (red arrows).  $T_1$  and  $T_2$  mark the regions used in  
 627 panel **b**. **b** Comparison of shifted mean-corrected FRET ratio at early times with no clear wavefront (top)  
 628 and distinctive traveling pulses at late times (bottom). **c** Comparison of the time dependence of the slope  
 629 for the case of added sperm DNA (+XS, orange) and control (-XS, green). Kernel density estimations  
 630 (normalized at each time) and LOWESS curves are given in the corresponding colors. **d** Time evolution of  
 631 the period (top) and wave speed (bottom) for +XS. **e** Speed-period relations for both conditions are obtained  
 632 from LOWESS curves in Fig. 1d (-XS) and Fig. 3d (+XS), respectively. Open circles (-XS) and open  
 633 squares (+XS) along the line highlight multiples of 100 minutes. The transition points are marked on dashed  
 634 guides for each, as done previously.



635 **Fig. 4 CSF boundary-driven mitotic waves.** **a** Schematic representation of the experimental setup to trigger  
 636 boundary-driven mitotic waves by a 5 second dip in CSF extract. **b** Solitary pulse of high Cdk1 activity  
 637 propagating with a speed of 40  $\mu\text{m}/\text{min}$  (wavefront indicated by a white line) in an interphase-arrested extract  
 638 triggered by CSF dipping. **c** Spatial profiles of the shifted FRET ratio from the kymograph in **b** showing the  
 639 excitable pulse. The red vertical line corresponds to CSF-induced arrest. **d** Kymographs for boundary-driven  
 640 traveling waves in cycling extracts without (left, -XS) and with nuclei (right, +XS) present. **e** Traveling  
 641 waves from kymographs in **d** revealed by the shifted mean-corrected FRET ratio without (-XS) and with  
 642 nuclei (+XS). **f** Wave speed as a function of time for the two conditions in panel **d** analyzed via later-time  
 643 exponential fits (red lines). **g** Speed-period relationship combining both LOWESS estimations for conditions  
 644 with (+XS) and without (-XS) nuclei. Transition points and guides are as previously defined.

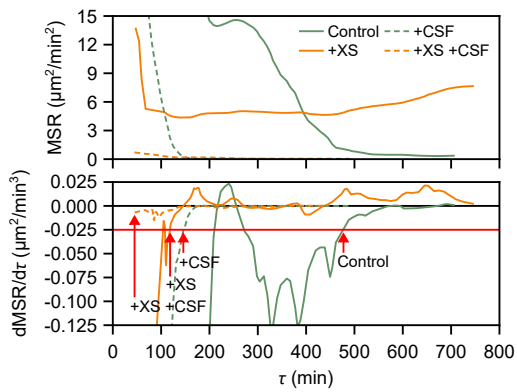


645 **Fig. 5 Influence of the oscillator properties and spatial heterogeneity on the formation of phase and**  
646 **trigger waves. a** Kymographs representing the spatiotemporal evolution of cyclin B-Cdk1 activity. (i)  
647 Simulation with a spatially homogeneous initial condition of activity and a spatially heterogeneous period  
648 dependence to introduce a pacemaker at  $x = 2.5$  mm, exhibiting trigger waves for  $\alpha = 1$ . (ii) Simulation  
649 with a spatially linear phase difference in the initial condition of activity and a spatially homogeneous period,  
650 exhibiting phase waves for  $\alpha = 1$ . (iii) Same spatial heterogeneity as (i) for  $\alpha = 0.1$ . (iv) Same spatial  
651 heterogeneity as (ii) for  $\alpha = 0.1$ . **b**  $v$  and  $\gamma$  as functions of  $\alpha$  resulting from fitting the long-term shapes of  
652 pacemaker-driven waves in **a** with the expression  $x = d + vt^\gamma$ , showing a progressive transition to linearly  
653 propagating trigger waves ( $\gamma = 1$ ) with a stable speed. **c** Temporal evolution with cycle number of the  
654 spatially averaged wave speed for phase and trigger waves in the shown kymographs (i) and (ii), panel **a**.  
655 Speed is measured only at the wavefront segments indicated in red lines.

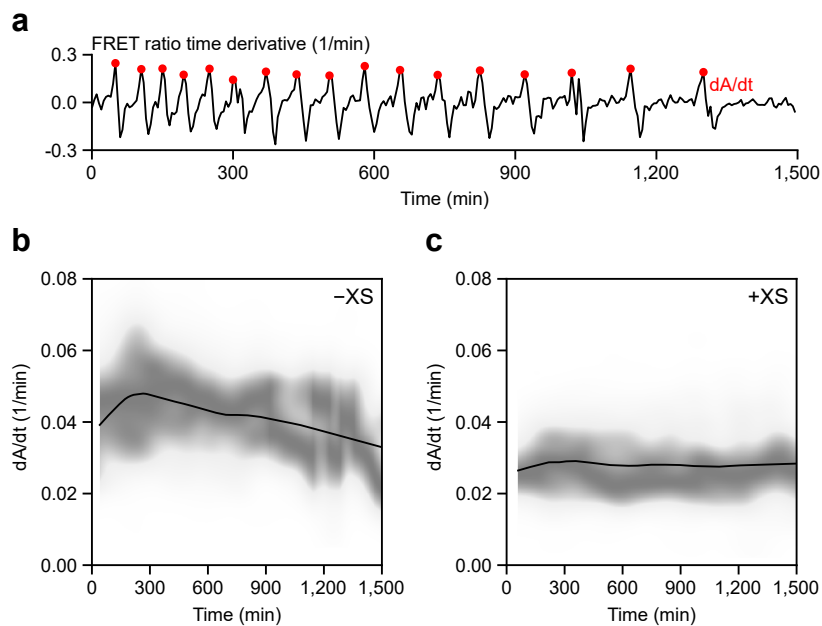


656 **Fig. 6 Spatial heterogeneity coordinates phase-to-trigger wave transition.** **a** Time evolution of wave  
657 speed. Each vertical line with the corresponding arrow on the top indicates  $\tau_0$  for each experimental condition  
658 (462, 115, 146, and 45 min for Control, +XS, +CSF, and +XS/+CSF, respectively). The horizontal line  
659 depicts the terminal for the excitable system ( $40 \mu\text{m}/\text{min}$ ). **b** Exponential relaxation of late-time wave speed.  
660 Time is measured from respective  $\tau_0$ , and speed is offset by the terminal speed and then normalized against  
661 the speed at  $\tau_0$ . The negative reciprocal of the curve slope gives a visual estimation of  $\Delta\tau$ , which are 528, 157,  
662 411, and 83 min for each condition. Dotted guidelines correspond to 50 and 500-min time scale relaxations,  
663 respectively. **c** Transition time scales  $\tau_0$  and  $\Delta\tau$  (top) and terminal speeds (bottom). Terminal speeds are  
664 44, 39, 27, and  $31 \mu\text{m}/\text{min}$  for each condition, converging to a similar level and comparable to the traveling  
665 speed of the activation pulse in interphase extracts driven by CSF ( $40 \mu\text{m}/\text{min}$ ).

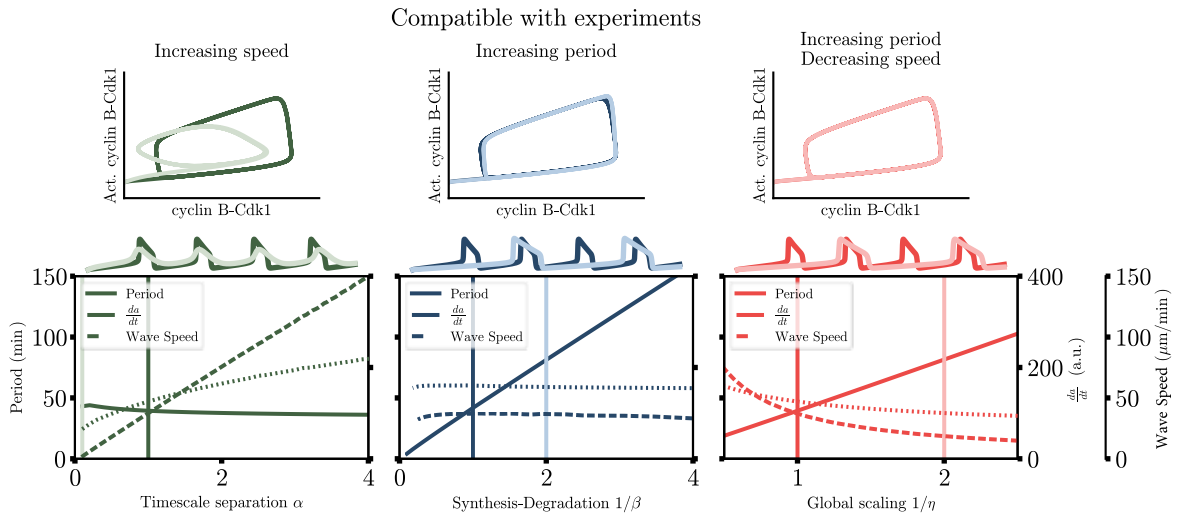
## SUPPLEMENTARY FIGURES



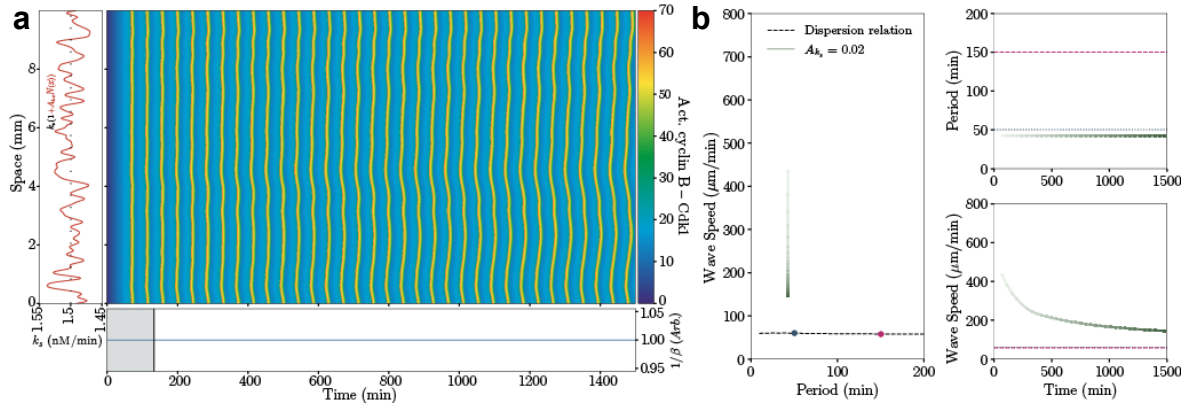
666 **Fig. S1** Mean square residual (MSR) of the exponential fitting of the wave speed at  $[\tau, \infty)$  (top), and its  
667  $\tau$ -derivative (bottom).  $\tau_0$  is defined as the largest  $\tau$  when the derivative is below a threshold (horizontal red  
668 line).  $\tau_0$  for each experimental condition is indicated with a red arrow.



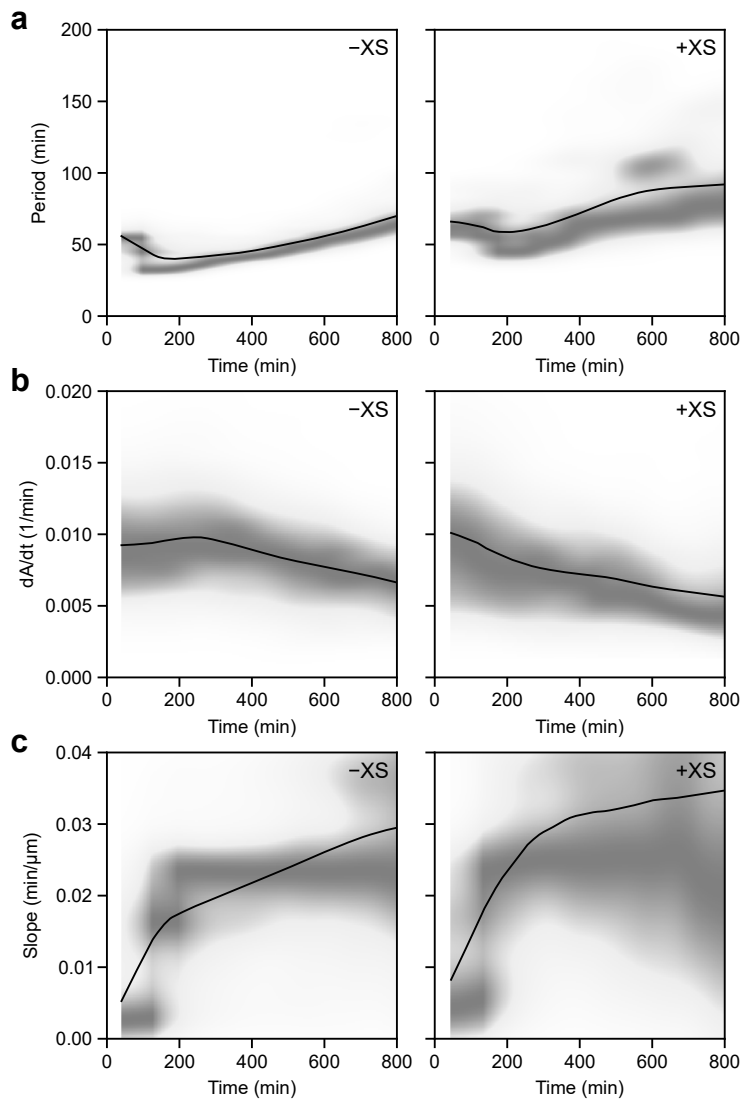
669 **Fig. S2 a** Definition of the maximum activation rate,  $dA/dt$ . The largest time derivative of FRET ratio per  
 670 cycle, indicated in red dots, is defined as  $dA/dt$ . The time course is taken at  $x = 10$  mm of the kymograph  
 671 given in Fig. 1b. **b** Maximum activation rate in non-driven experiments without sperm DNA ( $-XS$ ),  
 672 represented by the kernel density (gray colormap) and LOWESS (solid black line) estimations. **c** Maximum  
 673 activation rate in non-driven experiments with sperm DNA ( $+XS$ ).



674 **Fig. S3** Dependence of the period,  $da/dt$ , and wave speed for different parameter scalings. Top: Phase space  
675 representation of the oscillator and the corresponding time series. Bottom: Period,  $da/dt$ , and wave speed is  
676 represented using continuous, dashed, and dotted lines as function of timescale separation  $\alpha$  (left), decreasing  
677 synthesis and degradation rates with  $\beta$  (middle), and all rates with  $\eta$  (right). Vertical lines indicate the  
678 parameter values used in the top panels with the respective colors.



679 **Fig. S4 a** Spatiotemporal evolution of the activity of cyclin B-Cdk1 showing the transition from phase to  
 680 trigger waves with constant period with time using the parameter  $\beta(t) = 1$  (bottom) and spatial variability in  
 681 the synthesis term. **b** Speed-period relation and temporal dependence of the period and wave speed of the  
 682 numerical simulation in panel **a**, and the theoretical dispersion relation using the parameter  $\beta$  to scan the  
 683 period (black dashed line) same as in Fig. 2 included for comparison.



684 **Fig. S5** Period, maximum activation rate, and slope for CSF boundary-driven mitotic waves. **a** Period for no  
 685 sperm DNA ( $-XS$ ) and added sperm DNA ( $+XS$ ) cases. Both columns feature the kernel density estimation  
 686 over time with solid lines representing the LOWESS estimation. **b** Maximum activation rate. **c** Slope.

## MOVIES

687 **Mov. 1 Cdk1 wave dynamics in extracts without nuclei.** Data shared with the kymograph in Fig. 1.  
688 (Top) Pseudo-color movie of spatiotemporal dynamics of Cdk1 activity in bulk extracts. Color scale as in  
689 Fig. 1. Early times exhibit phase waves which give way to trigger waves over time. (Bottom) Detrended and  
690 smoothed FRET ratio (averaged over the width of the tube) plotted across the length of the tube. This shows  
691 how the spatial profiles develop from diffuse phase waves to pulse-like trigger waves.

692 **Mov. 2 Wave dynamics in extracts with reconstituted nuclei.** Data shared with the kymograph in Fig. 3.  
693 (Top) Pseudo-color movie of spatiotemporal dynamics of Cdk1 activity in bulk extracts. Color scale as in  
694 Fig. 3. Early times exhibit phase waves which quickly give way to trigger waves emanating from nuclei.  
695 Nuclei appear as hot-colored regions due to their import of active Cdk1. (Bottom) Detrended and smoothed  
696 FRET ratio (averaged over the width of the tube) plotted across the length of the tube. The curve represents  
697 the average over the width of the tube.

698 **Mov. 3 Excitable pulse in interphase extract driven by CSF.** Data shared with the kymograph in Fig. 4b.  
699 (Top) Pseudo-color movie of excitable pulse of Cdk1 activity in interphase extract as driven by CSF. (Bottom)  
700 Detrended and smoothed FRET ratio (averaged over the width of the tube) plotted across the length of the  
701 tube. A singular pulse is driven by the source.

702 **Mov. 4 CSF-driven wave dynamics in extracts without nuclei.** Data shared with the kymograph in Fig. 4d,  
703 left. (Top) Pseudo-color movie of trigger wave pulses in cycling extracts as driven by CSF. Phase wave  
704 dynamics are permanently abolished by driving. (Bottom) Detrended and smoothed FRET ratio (averaged  
705 over the width of the tube) plotted across the length of the tube. The curve represents the average over the  
706 width of the tube. The CSF source drives multiple trigger wave pulses.

707 **Mov. 5 CSF-driven wave dynamics in extracts with reconstituted nuclei.** Data shared with the kymograph  
708 in Fig. 4d, right. (Top) Pseudo-color movie of trigger wave pulses of Cdk1 activity in cycling extracts with  
709 reconstituted nuclei as driven by CSF. Both nuclei and the source drive trigger waves, but the CSF source  
710 ultimately dominates. (Bottom) Detrended and smoothed FRET ratio (averaged over the width of the tube)  
711 plotted across the length of the tube. The curve represents the average over the width of the tube.